Optimization of the strength vs. conductivity trade-off in an aluminium alloy designed for laser powder bed fusion

Melek Genc, Pierre Eloi, Jean-Jacques Blandin, Céline Pascal, Patricia Donnadieu, Frédéric de Geuser, Pierre Lhuissier, Christophe Desrayaud, Guilhem Martin

Optimization of the strength vs. conductivity trade-off in an aluminium alloy designed for laser powder bed fusion

Melek Genk[a,b], Pierre Eloi [b], Jean-Jacques Blandin[a], Céline Pascal[a], Patricia Donnadieu[a], Frédéric De Geuser[a], Pierre Lhuissier[a], Christophe Desrayaud[c], Guilhem Martin[a,*]

[a] Université Grenoble Alpes, CNRS UMR 5266, Grenoble INP, Laboratoire SIMaP, Grenoble, 38000, France

[b] THALES AVS France SAS, 25, rue Jules Védrines, F-26000 Valence, France

[c] Ecole des Mines de Saint Etienne, SMS, Physique et Mécanique des Matériaux (PMM), 158 Cours Fauriel F-42000 Saint Etienne, France

***corresponding author:** guilhem.martin@simap.grenoble-inp.fr

Abstract

The 6061 Al alloy in its T6 conditions is often considered a good candidate for applications requiring a good balance between strength and thermal conductivity. However, this alloy is often very difficult to process using laser powder bed fusion (PBF-LB) because of the development of hot cracks during fabrication. Here, we show that adding 2.3 wt.% of Zr to the 6061 heritage alloy makes it processable by PBF-LB (suppression of hot cracks). Hot crack mitigation is attributed to grain refinement. However, the addition of 2.3 wt.% of Zr greatly affects the microstructure and thus the mechanical and electrical/thermal properties of the Zr-modified 6061 alloy. Consequently, there is a need to design heat treatments to achieve a trade-off between yield strength and thermal conductivity. In this work, we designed two heat treatment sequences aiming at achieving such a trade-off: an adapted T6 sequence (550°C/30 min+ 180°C/4h) and direct ageing at 400°C/4h. On the basis of a multiscale microstructural study using optical microscopy, X-ray diffraction, and electron microscopy, we clarify the evolution of the microstructure induced by the designed heat treatments. The mechanical properties (hardness, tensile behavior) and thermal conductivity derived from electrical conductivity measurements are then discussed in light of the microstructural evolutions. The as-fabricated Zr-modified 6061 alloy shows a higher yield strength (370 MPa) than the heritage 6061 alloy in its T6 condition (260 MPa) but its thermal conductivity is found to be much lower (98 vs. 173 W/m.K). The two heat treatment sequences designed in this work enable the mechanical properties of the heritage 6061 alloy to be outperformed (yield strength of 350 and 460 MPa for the T6 and direct ageing heat treatment respectively) while maintaining an acceptable level of thermal conductivity (150 and 170 W/m.K for the T6 and direct ageing heat treatment respectively).

Keywords : Al-alloy ; Laser Powder Bed Fusion (PBF-LB) ; Microstructure; Mechanical Properties: Thermal conductivity

1. Introduction

Additive manufacturing turns out to be an interesting processing route to produce heat exchangers because it enables the fabrication of sophisticated geometries including internal channels [1]. 6XXX-series Al alloys are often considered good candidates for heat exchangers because they exhibit a good balance between mechanical strength and thermal conductivity in their T6 conditions. However, precipitation strengthened Al alloys, especially from the 6XXX-series, have been known for years to be sensitive to hot cracks during welding operations, see e.g. [2,3] As expected from the welding literature, processing the 6061 grade by laser powder bed fusion (PBF-LB [4]) has been shown to be very challenging as severe solidification cracking occurs [5,6]. This cracking sensitivity prevents the 6061-alloy from being used in heat exchangers fabricated by additive manufacturing. Two main strategies have been proposed to overcome this hot cracking issue.

The first strategy relies on process optimization to decrease thermal stresses, typically by introducing a high-temperature preheating stage before melting as suggested in [7]. However, this would require machines allowing to achieve high preheating temperatures (> 400°C) and would not permit to take full advantage of the high solid-liquid interface velocities typical of PBF-LB to achieve supersaturated solid solutions due to solute trapping or to form strengthening metastable phases.

The second strategy also inherited from the welding community consists in refining the grain size. Different methods are efficient in achieving grain refinement in Al alloys processed by additive manufacturing.

The addition of extra particles such as LaB_6 [8] or TiB_2 [9,10] acting as direct nucleating agents thanks to a small misfit between such particles and the Al matrix has been successfully used. In this case, the initial powder batch is mixed with the particles, and those particles do not contribute much to directly strengthening the alloy (indirect effect through grain boundary strengthening).

An alternative to this approach consists in mixing the initial powder batch with another powder made of nanoparticles: Zr-hydrides [11,12], or Zr-containing oxides [13,14]. Reactions during the process allow the introduction of zirconium in the liquid promoting the formation of primary $L1_2$-structured Al_3X phases known to have a small misfit with the Al matrix [11,15,16]. An attempt to clarify the microstructure-strength relationships in a 6061 alloy modified with the addition of Yttria-Stabilised Zirconia (YSZ) has also been very recently proposed in [17]. However, the compromise between strength and thermal/electrical conductivity was not investigated. In addition, the solution consisting in functionalizing powder with nano-sized particles suffers from safety issues due to nanoscale particle handling.

Another pathway toward grain refinement consists of the introduction of solutes beforehand that promote the precipitation of primary phases in the liquid, increasing the number of heterogeneous nucleation sites. This strategy shows the advantage of not requiring a powder mixing step after powder atomization. Zr and Sc have been successfully added to form primary $L1_2$-structured Al_3X phases exhibiting a small misfit allowing such primary phases to act as nucleation sites during PBF-LB, see examples in [15,18–23]. More recently Nb [24] and Ti [25] have also been identified as possible candidates to refine the grain size of additively manufactured Al alloys. Such a strategy is also promising because the processing conditions typical of PBF-LB can be exploited to achieve supersaturated solid solutions that can be further heat-treated to increase the mechanical strength while increasing the electrical or thermal conductivity. Introducing Zr in heritage Al alloys to improve their processability via AM has already been proposed in the literature, see examples on 5XXX [26], 6XXX [13,27], or 7XXX series [28]. Mehta et al. [27] reported successful attempts to produce crack-free samples in a Zr-modified 6061 (addition of 1 wt.% Zr). The same authors have also investigated the tensile properties of the as-fabricated microstructure as well after a T6 sequence but the

microstructure-property relationships have been poorly addressed, in particular functional properties were not investigated.

The objective of the present work is to alter the chemical composition of the heritage 6061 Al-alloy to ensure its processability via PBF-LB (no hot cracks) while improving the trade-off between mechanical strength and thermal conductivity. Post-fabrication heat treatments are designed such as to take advantage of the processing conditions typical of PBF-LB (high solid-liquid interface velocities and high cooling rates) in order to tune the strengthening contributions of different precipitates while increasing the thermal conductivity. We shed light on the mechanisms responsible for the evolution of mechanical properties and thermal conductivity revealing that Zr-addition strongly modifies the metallurgy of the 6061-alloy.

2. Experimental Procedures

2.1. Alloy modification, powder atomization and powder characteristics

To make the 6061 alloy processable by PBF-LB, a pre-alloyed powder of a standard 6061 was gas atomized but with a substantial addition of Zirconium, about 2.3 wt. %, twice more than in the work of Mehta [27] and Opprecht [17]. This alloy will be qualified as a Zr-modified 6061 alloy in the subsequent sections. The introduction of zirconium was employed to refine the microstructure and thus mitigate hot cracking due to the formation of primary $L1_2$-structured Al_3Zr- precipitates exhibiting a small lattice parameter misfit compared to the Al matrix and having a cubic shape morphology. Zr was chosen rather than Sc additions because of cost-efficiency considerations and also because Zr is a slower diffuser than Sc. As Zr is a slow diffuser in the Al matrix, a highly supersaturated solid solution can be retained in the as-fabricated conditions due to the typical processing conditions of PBF-LB, offering the possibility of further strengthening the material via a post-fabrication direct ageing treatment while increasing the thermal conductivity. In this case, the out-of-equilibrium processing conditions are exploited to limit post-fabrication heat treatments because solutionizing can be avoided.

Regarding the Zr content added in the Zr-modified 6061 alloy, we relied on a previous work that was dedicated to investigating the amount of Zr required to achieve crack-free parts [29,30]. In this study, a powder batch of the standard 6061 alloy was mixed in different proportions with a powder batch of a binary Zr90-10Al wt.% alloy to adjust the overall Zr content, respectively to 1, 2, and 5 wt.%. It was concluded from this work that a Zr content of ≈ 2 wt.% was necessary to produce consistently crack-free parts as few cracks were still observed in the parts fabricated using a mixture with 1 wt.% of Zr [29,30]. As a result, we imposed a minimum Zr content of 2 wt.% during powder atomization. However, it has to be highlighted here that this 2 wt.% addition of Zirconium was determined using the powder mixture as the powder feedstock for PBF-LB. Thus, one can suspect local chemical inhomogeneities during the process because of the difference in liquidus temperature between the 6061 alloy and the Zr-10Al alloy leading to the development of a few cracks in regions depleted in zirconium. This critical Zr content is likely to differ if a pre-alloyed powder was to be loaded into the PBF-LB machine instead. Indeed, the recent work of Mehta *et al.* [27] suggests that introducing 1 wt.% of Zr is enough to overcome hot cracking issues when using a building substrate maintained at 100°C.

The powder batch was atomized under Ar by Nanoval®. The chemical composition of the as-received powder batch was measured by Electrowerk Weisweiler GmbH and is given in **Table 1** along with the standard composition of a 6061 alloy and the targeted composition of the Zr-modified 6061 alloy. Overall, the produced powder batch matches relatively well our initial requirements for most solutes except for Si and Mg, two of the major alloying elements added to the 6061 alloy to allow strengthening through the precipitation of the β' and β'' metastable phases. Indeed, the Si content exceeds the standard > 0.8 wt.% while the Mg content is slightly lower (0.76 wt.%) than the lower bound imposed by the standard (0.8 wt.%). This modification of the Mg/Si ratio may be significant for the formation of (Mg, Si) rich precipitates [31–33]. Furthermore, the oxygen content in the powder was found to be substantially higher (0.14 wt.%) than in standard wrought products where it is typically found < 0.05 wt.%. This is not surprising given the high surface-to-volume ratio of powder particles. Finally, with a Zr content of 2.3 wt.%, the powder composition is in agreement with the target value. Overall, it is important to highlight that the as-received powder batch of the Zr-modified 6061 alloy, though partially based on the heritage 6061 alloy, cannot be strictly considered to belong to the 6XXX-series since Zr is the largest solute addition. Thus, even if this modified version will be qualified as a Zr-modified 6061 alloy for the sake of clarity, one has to keep in mind that the designed alloy is far from being an Al-alloy from the 6XXX-series.

	Al	Si	Mg	Fe	Cu	Cr	Ti	Zn	Mn	Zr	O*
Alloy 6061 ASTM Standard [34]	Bal.	0.4-0.8	0.8-1.2	< 0.2	0.15-0.4	0.04-0.35	< 0.15	< 0.25	< 0.15	/	< 0.05
Zr-Modified 6061 (target)	Bal.	0.4-0.8	0.8-1.2	< 0.2	0.15-0.4	0.04-0.35	< 0.15	< 0.25	< 0.15	2.0-2.5	< 0.05
Zr-Modified 6061 (powder)	Bal.	1.02	0.759	0.280	0.348	0.105	0.064	0.012	0.103	2.29	0.14
Zr-modified 6061 (bulk)	Bal.	1.04	0.684	0.299	0.354	0.115	0.058	0.010	0.105	2.33	0.068

*Table 1. Chemical composition given in wt.% of the Ar-atomized powder batch of the Zr-modified 6061 alloy. The chemical composition of the standard 6061 alloy is given for comparison. All elements were measured by Inductively Coupled Plasma optical spectrometry (DIN 51008-2, DIN 51009), except O which was measured by *Infrared method after fusion under inert gas (ASTM E 1409).*

The morphology of the as-received powder batch was characterized by electron microscopy using a ZEISS GEMINI SEM500 field emission gun scanning electron microscope (FEG-SEM). The as-received powder exhibits a spherical morphology with numerous satellites and agglomerates, see **Figure S 1**. The particle size distribution was measured by laser diffraction (Malvern Mastersize 2000) giving a Dv_{50} equal to 25 µm. The powder flowability was characterized by measuring the Hausner index H defined as the ratio between the freely settled bulk density of the powder and the tapped bulk density of the powder. The latter one was measured to be H = 1.22 which corresponds to a fair flowability based on the classification suggested in [35].

2.2. PBF-LB processing conditions

Samples were produced using a ProX200 PBF-LB machine from 3D systems equipped with a Yb-laser (1070 nm wavelength). The building substrate was a 10mm-thick plate made of a 5XXX Al-alloy and was not preheated. Fabrication takes place under an Argon flow so as to keep the oxygen content below 500 ppm throughout the build. Two kinds of sample geometries were fabricated: 10 × 10 × 10 mm^3 cubes and 10 mm diameter cylinders with a length of 60 mm. Cylinders were built horizontally with their length parallel to the X or Y direction, X and Y defined as the system coordinates of the building substrate, and the Z-axis parallel to the building direction (BD) as indicated in **Figure S 2a**.
All samples were fabricated using the same set of processing parameters given in **Table 2** and resulting in a volumetric energy density (VED) of almost 80 J/mm^3. The scanning strategy consists of melting hexagonal islands as schematically shown in **Figure S 2a.** The fabricated cubes and cylinders on the building substrate are shown in **Figure S 2b**. The chemical composition of the as-fabricated parts was also measured and is reported in **Table 1**. We noticed a slight decrease in the Mg content in the parts, probably because of Mg evaporation during PBF-LB. No stress-relief treatment was applied before removing the samples from the building substrate.

Power P (W)	Speed v (mm/s)	Hatch spacing h (µm)	Layer thickness e (µm)	Volumetric Energy Density (J/mm^3)
285	1700	70	30	79,8

Table 2. Processing parameters employed to build samples by PBF-LB.

2.3. Heat treatments

As-fabricated samples were subjected to various heat treatments under air including direct ageing at 400°C or 180°C, without a solutionizing heat treatment to take full advantage of the processing conditions. Other as-fabricated samples were subjected to a typical 6061 alloy T6-heat treatment consisting of a solutionizing heat treatment at 550°C for 30 min and water quenching followed by ageing at 180°C. The solutionizing annealing time was shortened (only 30 min) because microsegregations develop at a much finer scale in PBF-LB in comparison to their cast counterpart. Additional samples were only subjected to the sole solutionizing treatment (550°C for 30 minutes + water quenching). Samples from the heritage 6061 alloy processed by the traditional cast and wrought processing route were also subjected to solutionizing followed by annealing at 400°C or a typical ageing treatment performed at 180°C for comparison with the Zr-modified 6061 alloy.

2.4. Density and defects characterization

The density of some as-fabricated samples was measured using image analysis based on optical micrographs and X-ray computed tomography (XCT). Five optical images were taken using an Olympus D27 microscope at different locations on 2D mirror polished cross-sections containing the building direction. The images were then converted into 8-bits and segmented to isolate pores using Fiji [36] (pores appear in black while the bulk material appears in white). The relative density was then estimated by averaging the results over the 5 images processed.

Some as-fabricated cube samples and tensile specimens prior to testing have also been scanned using X-ray computed tomography (XCT) to characterize the defect distribution. A Easytom-XL from RX-Solutions was used using a voxel size of 9 µm. 3D volumes were reconstructed with the Xact software using a standard filtered back-projection algorithm. The 3D image was first converted to 8-bits and then processed using a 3D Median filter (radius of 2 pixels). Finally, the 3D image was manually segmented to isolate defects. Given the voxel size employed, objects with a diameter smaller than 20 µm cannot be detected.

2.5. Microstructural characterization

Microstructural investigations have been carried out by combining several techniques depending on the scale of interest. Investigations at sub-millimeter and micron scales were respectively performed with an opto-numerical Olympus DSX500 microscope and a Zeiss SUPRA 55VP FEG equipped with an EDXS (Energy-dispersive X-ray spectroscopy) and an EBSD (Electron Back Scattered Diffraction) detector. Sample surfaces have been mechanically ground using SiC abrasive papers down to the P2400 grade followed by two polishing steps with successively a 3 and 1 µm diamond suspension. A final polishing step was applied using a 0.04 µm- aqueous colloidal silica solution. The microstructure at the melt pool scale was revealed by chemical etching using Keller reagent for 1 minute. Samples characterized by EBSD were subjected to a 12h polishing using the VibroMet Buehler device. Low-magnification EBSD maps were acquired using a step size of 1 µm while high-magnification EBSD maps were collected using a step size of 100 nm. SEM-EDSX measurements were performed using an accelerating voltage of 10 kV at a working distance of 10 mm.

X-Ray Diffraction (XRD) was performed on samples produced by PBF-LB with a PANalytical X'PERT MPD instrument equipped with a 1D linear X'Celerator detector and a copper source (λ = 1.5041 Å). The indexing of the diffraction patterns was done using the ICDD PDF4 + database.

To characterize the microstructure at the micro/nano scale, transmission electron microscopy (TEM) was carried out on thin foils prepared by electropolishing with a Tenupol 5 using a solution consisting of 20% Nitric acid and 80% methanol at -25°C and 25 V. TEM conventional bright-field (BF) and dark-

field (DF) images were acquired on a JEOL 3010 transmission electron microscope operating at 300 kV. The Energy-dispersive X-ray spectroscopy (EDXS) has been carried out on a TEM FEG JEOL 2100 operating at 200 kV using a high collection angle SDD Centurio detector. In the present work, the TEM-EDXS results are considered only for relative comparisons. In the different regions identified at the melt pool scale, ACOM (Automated Crystallographic Orientation Mapping) was performed with the hardware and software toolset ASTAR TM from Nanomegas to retrieve the local orientation information. The details of this technique are given in [37]. In summary, a nano-beam is scanned over the area of interest and, at each point of the scan, diffraction patterns are acquired with a CCD camera. By post-processing the diffraction data sets, the phase orientation at each position is assigned by comparison to simulated patterns of candidate phases using a template matching technique, see [20,37,38] for more details. Note that owing to the small probe size (typically 1-2 nm) and small step size (typically 10-50 nm), the ACOM method provides high spatial resolution maps.

Additional characterization of the nanoscale precipitation was provided by differential scanning calorimetry (DSC) experiments. For this, samples were mechanically cut to roughly 3 mm x 3 mm x 1 mm slabs (about 25 µg in mass). They were subjected to a 20 K/min heating ramp from -20°C to 600°C in pure aluminium crucibles with an empty reference crucible in a Mettler-Toledo DSC 3+ instrument. To further highlight the enthalpic transitions, a polynomial baseline was subtracted. It was obtained by considering the 0°C-50°C and 550°C-600°C (after solvus) temperature ranges where we assumed no transition happened.

2.6. Mechanical characterization

Vickers hardness measurements were carried out using a FALCON 400 INNOVA-TEST device in the XZ cross-sections with a load of 10 kgf and a dwell time of 10 s. For each condition, at least 10 measurements were performed and the average value was computed. The error was estimated by computing the standard deviation.
Tensile tests were conducted at a constant strain rate of 10^{-4} s^{-1} using a DY35 ADAMEL mechanical testing machine equipped with a 20 kN load cell. Cylindrical tensile specimens with a gauge length of 24 mm and a diameter of 4 mm were extracted from the as-fabricated cylinders shown in **Figure S 2b**. At least 3 specimens of each build orientation (X and Y) were deformed to fracture. Strains were recorded throughout the tensile tests by digital image correlation using ARAMIS® GOM Correlate software based on a speckle deposited on the surface specimens prior to straining.

2.7. Electrical and thermal conductivity measurements

The electrical conductivity of the specimens was estimated using the Eddy current method. This method consists in applying an alternating magnetic field with a frequency f using a probe in contact with the sample to create the so-called Eddy current perpendicularly to the axis of the probe. A NORTEC 600 from Olympus equipped with an 8 mm probe was employed, and the frequency was set to 480 kHz. The probe was applied at least three times on two different polished cross-sections, respectively on the XY and XZ cross-sections. The conductivity σ is given in %IACS (100%IACS = 58 MS/m). First, it is important to recall that in well-conductive metals such as aluminium and its alloys, the conductivity is mainly electronic and the contribution from phonon is negligible. This is why the thermal conductivity λ_{th} can be deduced from the electrical conductivity σ measurements based on the Smith-Palmer formula [39]: $\lambda_{th} = 0.869 L_0.T.\sigma + 11.2$ with T the temperature is given in Kelvin and L_0 the Lorentz number $L_0 = 2.44 \times 10^{-8}$ $W.\Omega.K^{-2}$. This formula is an extension of the Wiedmann-Franz-Lorentz law ($\lambda_{th} = L_0.T.\sigma$) and was validated for various Al alloys including the 6061 alloy [39] which is the material of interest in this work. The error was estimated by taking the maximum variation with respect to the average value over the three measurements. Such measurements will also provide interesting insights regarding the solid solution since the presence of solute is known to affect the electrical conductivity, see e.g. [39,40].

3. Experimental Results

3.1. Density and defects

Optical cross-sections taken in the XZ-plane as shown in **Figure 1a** reveals the absence of cracks parallel to the build direction in the as-fabricated parts demonstrating that crack mitigation was successfully achieved in this Zr-modified 6061 alloy. The mechanism at the origin of cracks mitigation was already well-documented in the literature, see e.g. [13,27]. Briefly, the nucleation of Al grains promoted by the precipitation of the primary Al_3Zr $L1_2$ phase along the melt pool boundary enables grain refinement. The nucleation of new Al grains at the bottom of the melt pool inhibits the growth of large columnar grains growing by epitaxy from the underlying layers, a situation known to promote the formation of hot cracks. Few residual defects are still observed and can be classified based on their size, morphology, and spatial distribution. Lack of fusion defects exhibit an irregular shape with the largest ones exceeding a few hundred of microns in size and often located in the inter-layer regions or in between adjacent molten tracks as illustrated in **Figure 1a**. Gas pores, inherited from the powder or generated by the keyhole effect [41], show a near-spherical morphology. As suggested by the morphology of the molten bead, see **Figure 1a,** samples were produced with parameters leading to a conduction regime. Thus, spherical pores are thought to mostly come from the initial powder and therefore rarely exceed 20-30 µm in diameter as the largest ones cannot be bigger than the largest powder particles. The latter idea is further supported by the characterization by XCT of the as-received powder particles that reveals the presence of spherical pores in some particles (in red in **Figure S 4**). The relative density measured by image analysis and XCT on an as-fabricated cube sample was respectively 99.4 and 99.9%.

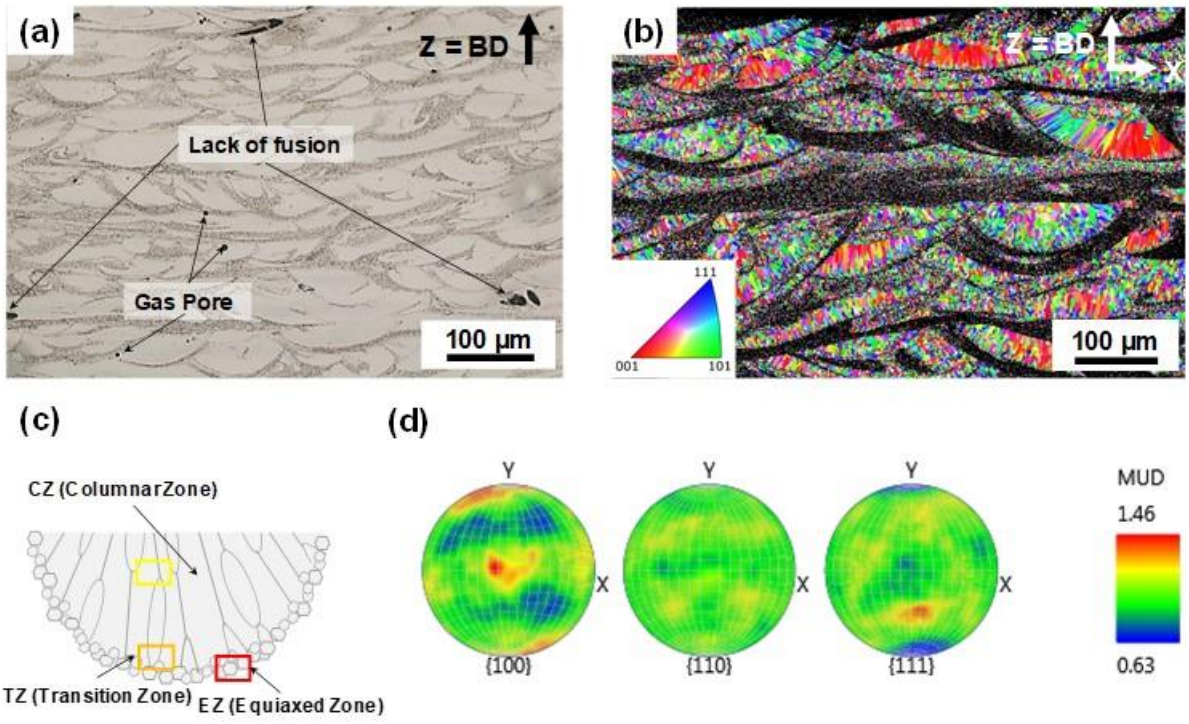

Figure 1. (a) Optical micrograph taken in the XZ-plane showing the absence of cracks propagating along the build direction. (b) Low-magnification EBSD IPF-Z map acquired in an XZ cross-section in an as-fabricated sample (step size 1 µm). (c) Schematic of the grain structure at the scale of the melt pool. (d) (100), (110) and (111) Pole figures plotted from the crystallographic orientations determined in (b). Colored rectangles correspond to the location of the SEM images displayed in ***Figure 2****.*

3.2. As-fabricated microstructure

The low-magnification EBSD-IPF map shown in **Figure 1b** provides an overview of the microstructure where multiple molten tracks can be easily distinguished. Note that the region along the melt pool boundaries were not properly indexed. Black regions in **Figure 1b** correspond to points where the confidence index was < 0.1. Such low indexing results from the step size employed to map such a large area (1 µm) which does not allow to resolve the fine equiaxed grains present along the melt pool boundaries. Contrary to the typical columnar grain structure elongated along the build direction and which grows through several layers due to epitaxial growth, as typically observed in a standard 6061 alloy [5] processed by PBF-LB, the grain structure of the Zr-modified 6061 is much finer.

At the scale of the molten pool, two regions can be distinguished as schematically shown in **Figure 1c**: a region located close to the boundary of the melt pool consisting of fine equiaxed grains with a typical size of nearly 500 nm (EZ = equiaxed zone); and a region made of fine columnar grains (several micrometers in width) in the upper part of the molten bead aligned in the direction of the thermal gradient (CZ = columnar zone). In the CZ, the grain size is refined compared to what has been reported for a standard 6061 fabricated by PBF-LB [5,7]. The microstructure can thus be considered as a composite made of equiaxed and columnar grains. Pole figures calculated based on the crystallographic orientations determined in the region analyzed in **Figure 1b** are given in **Figure 1d** to evaluate the texture. Though a lot of points located in the EZ could not be indexed properly with the step size employed here (100 nm), the pole figures suggest that the addition of Zr leads to texture randomization, the maximum intensity being only about 1.5 in the (100) pole figure. Only a few regions in the CZ still exhibit a (100) texture (grains displayed in red in **Figure 1b**).

Figure 2a-c shows SEM-BSE micrographs acquired in, respectively, the EZ, transition zone (TZ), and columnar region (CZ) as indicated in the schematic shown in **Figure 1c**. The most striking feature is the presence of numerous intermetallic particles regardless of the region of interest, with a possibly larger fraction in the EZ. In the EZ, particles are distributed either in the grain center (precipitates with a cube-like morphology), or in the intergranular regions with more irregular morphology. The cubic-like precipitates are not observed in the CZ where the particles are exclusively found in the intercellular (no development of dendrite secondary arms) or intergranular regions. The image acquired in the TZ reveals that there is a sharp interface between the EZ and the CZ.

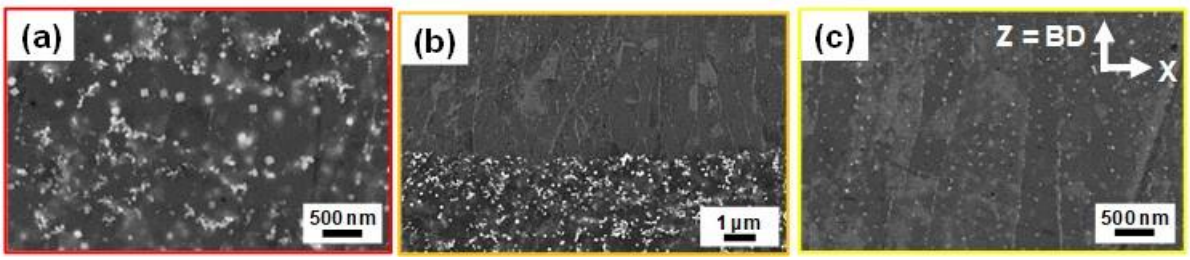

Figure 2. SEM-BSE micrographs taken in different regions of interest: (a) in the EZ ; (b) in the TZ ; (c) in the CZ.

Each zone was then characterized down to the nanoscale using TEM-BF imaging and EDXS maps collected in the same region of interest to detect solutes trapped in the various intermetallics. **Figure 3a** and **Figure 3b** give an overview of the microstructure respectively in the EZ and CZ. The cubic-shaped precipitates, already reported in the literature (see, e.g. [15,19,23]) and located in the center of some equiaxed grains (see black arrow in the STEM-BF image shown in **Figure 3a**) are rich in Zr (EDXS map in **Figure 3a**) but depleted in other solutes. They can be attributed to the primary metastable Al_3Zr phase (identified on the XRD pattern in **Figure S 5**) acting as a nucleating agent for the Al matrix and being responsible for grain refinement. A variety of other intermetallic particles are found decorating the grain boundaries. Those are rich in different solutes, especially Fe, Si, and Mg, and to a lesser extent Mn and Cu. Small nanoscale oxides were also detected. **Figure 3b** confirms the absence of the primary phase with a cubic shape morphology in the CZ. Interestingly, no intermetallic particles rich in Zr are

detected at this scale in the CZ due to solute trapping induced by the high solid-liquid interface velocities in the upper region of the melt pool, see e.g. [15]. Solutes such as Fe, Mg, and Si are trapped in intermetallic particles distributed in the interdendritic or intergranular region forming strings aligned with the dendrite growth direction. On this scale, local enrichment in Cu and Mn is hardly evidenced. Tiny oxides are also detected in the EZ. The transition zone was also analyzed by coupling EDXS mapping with ACOM to appreciate the grain structure of the Al matrix in each zone and evaluate the differences in local Zr enrichment. The crystallographic orientation map helps to appreciate the size of the grains, the equiaxed grains having an average diameter of nearly 500 nm while the width of the columnar grain is about 1-2 µm. The EDXS map reveals a substantial difference with respect to the distribution of Zr in the EZ and CZ, respectively. This is even better illustrated in **Figure 4** which shows a STEM micrograph taken in the TZ (**Figure 4)** where an EDXS map of Zr (**Figure 4b**) was collected and a crystallographic orientation map was acquired (**Figure 4c**). A lot of intermetallic particles are enriched in Zr in the EZ but none could be detected in the CZ at this scale.

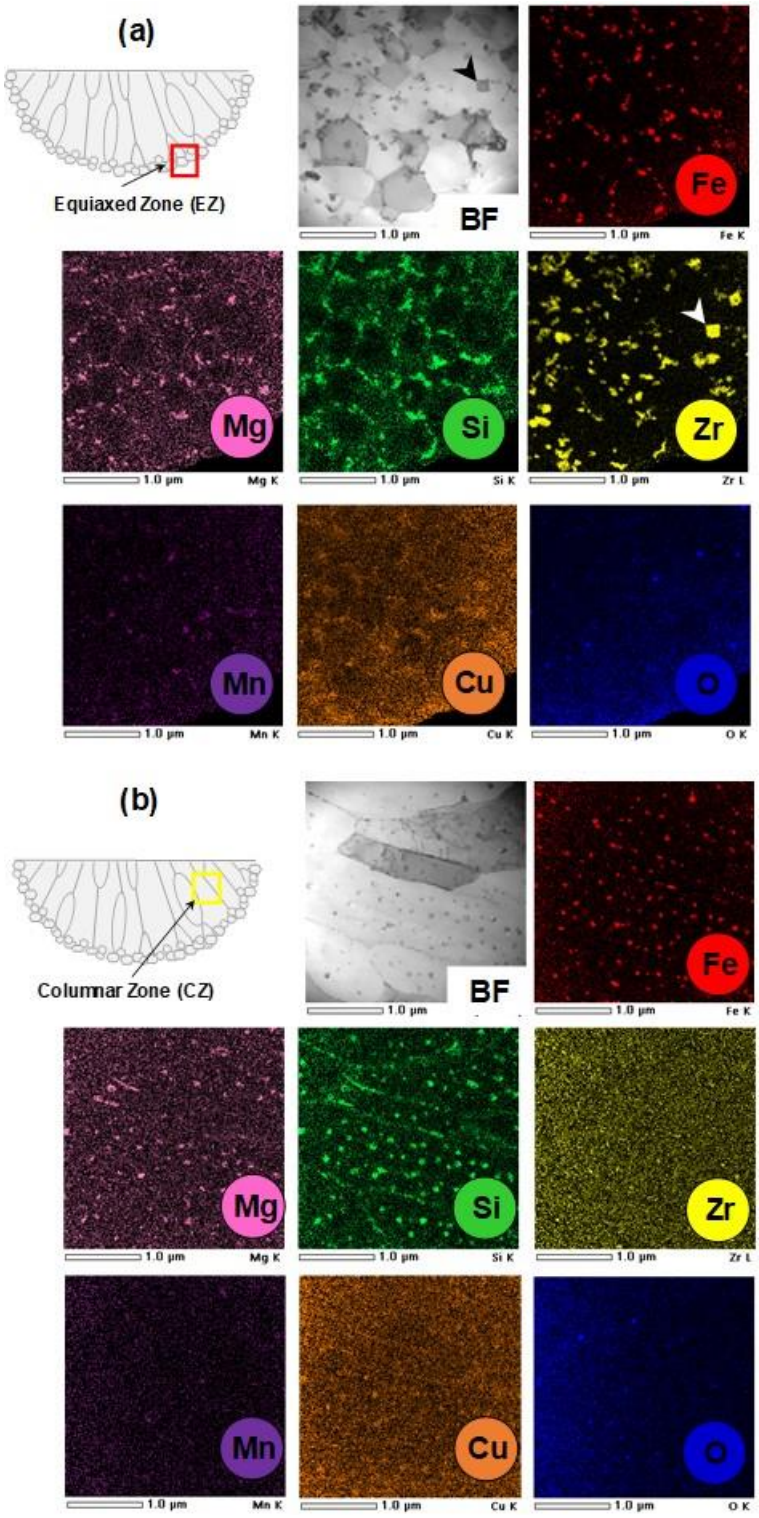

Figure 3. Overview of the as-fabricated microstructure revealed by STEM and EDXS mapping (a) in the EZ and (b) in the CZ.

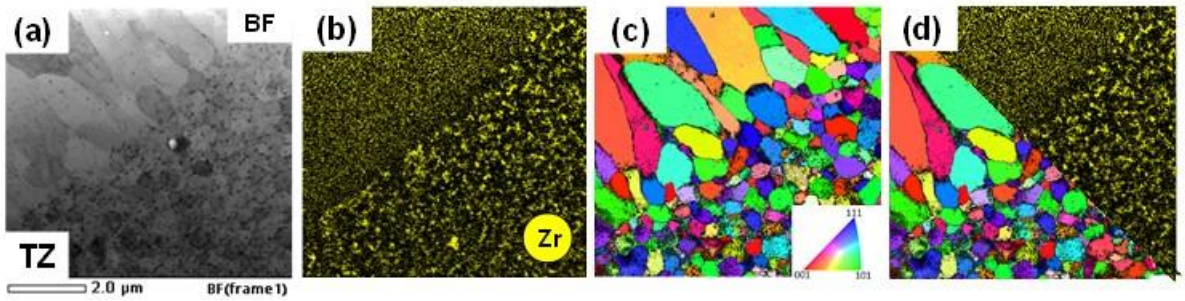

Figure 4. (a) TEM image of the transition zone (TZ). (b) EDXS map of Zr acquired in the same region of interest (STEM mode). (c) Crystallographic orientation map of the Al matrix acquired by ACOM in the same region of interest. (d) Summary of the results shown in (a), (b) and (c).

3.3. Post-fabrication heat treatments: microstructure and hardness evolutions

3.4.1. Standard T6-sequence

Some as-fabricated Zr-modified 6061 samples were first subjected to a T6-sequence consisting of solutionizing at 550°C/30 min followed by ageing at 180°C/4h. This treatment mimics what is usually used to strengthen the standard cast and wrought 6061 alloy by nanoprecipitation of the β' and β'' metastable phases. Given the processing conditions of PBF-LB that could result in a supersaturated solid solution, we also subjected the as-fabricated material to direct ageing at 180°C. In parallel, a standard wrought 6061 was subjected to a solutionizing heat treatment at 550°C/2h followed by ageing at 180°C (T6) to highlight the differences with the Zr-modified 6061 processed by PBF-LB. **Table 3** summarizes the hardness and thermal conductivities measured after different heat treatments. After solutionizing at 550°C for 30 min, the hardness of the Zr-modified 6061 alloy drops to 85 HV in comparison with the as-fabricated conditions (about 115 HV) while the thermal conductivity increases from about 98 W/m.K in the as-fabricated conditions to 160 W/m.K after solutionizing. After completion of a T6 sequence (ageing at 180°C for 4h after solutionizing), the hardness of the Zr-modified alloy substantially increases in comparison to the solutionized conditions to reach 124 HV, and the thermal conductivity further increases to nearly 170 W/m.K, see **Table 3**.

	Hardness Vickers (HV)	**Thermal conductivity* (W/m.K)**
Zr-modified 6061 Alloy (Zr = 2.3 wt.%) This work		
As-fabricated	116 ± 1	98 ± 2
Solutionized (550°C/30min)	85 ± 2	160 ± 2
T6 (550°C/30min + 180°C/4h)	124 ± 2	170 ± 2
Direct aged 180°C/4h	120 ± 2	101 ± 2
Standard cast and wrought 6061 Alloy		
Solutionized (550°C/2h)	55 ± 1	164 ± 2
T6 (550°C/2h + 180°C/4h)	116 ± 2	173 ± 2

*Table 3. Summary of the hardness and thermal conductivity measured on samples subjected to various post-fabrication heat treatments. *Deduced from electrical conductivity measurements.*

The hardness and thermal conductivity evolutions upon ageing at 180°C are respectively given in **Figure 5a** and **Figure 5b** for both the Zr-modified and standard cast and wrought 6061 alloy. For the Zr-modified 6061 alloy, after direct ageing at 180°C, the evolutions of both hardness and thermal conductivity are not significant, see **Figure 5a-b**. In **Figure 5a**, the hardness peak is barely visible but a slight hardness increase can be detected after 180°C/1h from 116 HV in the as-fabricated conditions

to 120 HV after 180°C/1h while the thermal conductivity slightly steadily increases from 98 W/m.K in the as-fabricated conditions to about 103 W/m.K (**Figure 5b**). A slight decrease of the hardness can be detected for ageing times longer than 1-2h. Similar measurements were carried out on a standard wrought 6061 alloy subjected to a solutionizing heat treatment at 550°C/2h followed by ageing at 180°C, see **Figure 5a-b**. The hardness of a standard cast and wrought 6061 alloy increases during the first 3 hours and reaches a peak between 3 and 10h (about 115 HV after 180°C/4h). At the same time, the thermal conductivity continuously increases with time and is about 173 W/m.K after 4h at 180°C and about 177 W/m.K after 24h at 180°C.

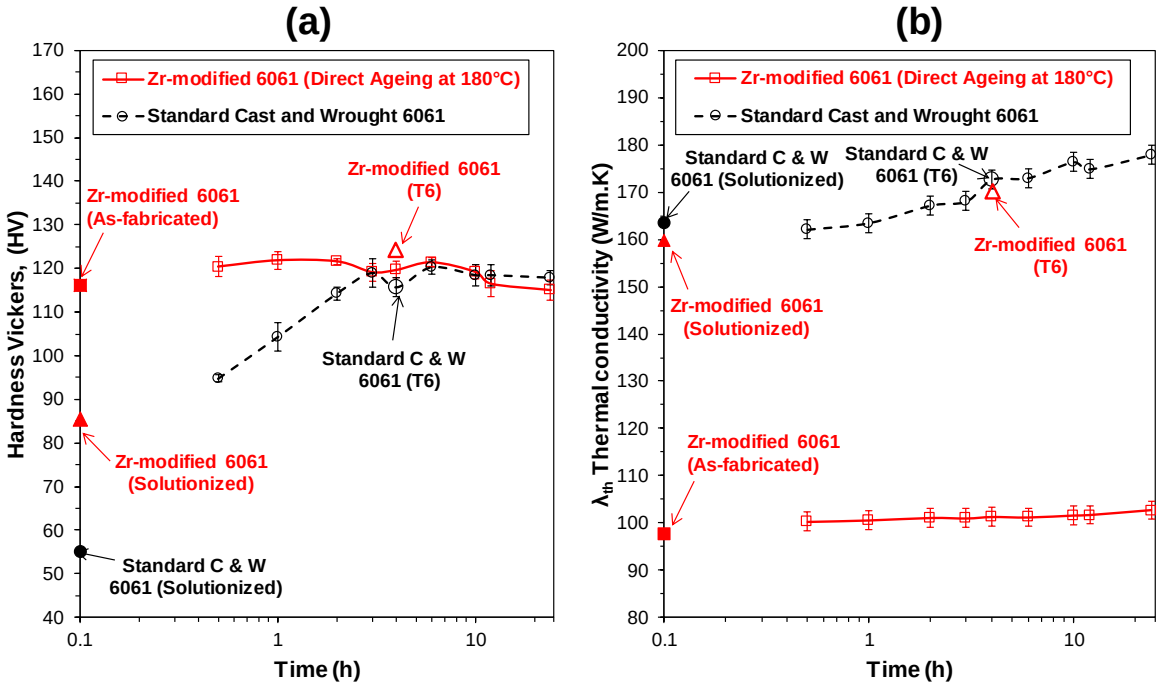

Figure 5. (a) Hardness and (b) thermal conductivity evolution with time after ageing at 180°C for both the Zr-modified and standard cast and wrought 6061 alloy.

The microstructures of the Zr-modified 6061 alloy were also characterized after solutionizing and after a full T6-sequence. Solutionizing at 550°C leads to a modification of the grain structure in comparison to the as-fabricated material, see the EBSD-IPF shown in **Figure 6**. A highly heterogeneous grain structure is observed after solutionizing with fine grains whose size was nearly unaffected in comparison with the grains detected in the as-fabricated material, and very large recrystallized grains with a size exceeding several hundreds of microns.

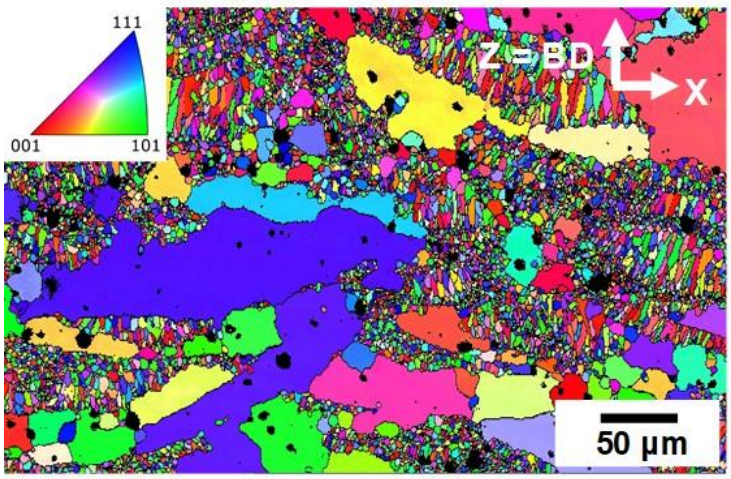

Figure 6. High-magnification EBSD-IPF map acquired a Zr-modified sample subjected to a solutionizing treatment at 550°C/30 min (step size 100 nm).

In addition to the Al matrix, two other phases can be identified on the basis of the XRD pattern collected from a sample subjected to 550°C/30 min: Al_2ZrSi and $Al_{19}Fe_4MnSi_2$, see Figure 7.**a-b**. The stable Mg_2Si phase was not detected in the XRD pattern. Note that no differences were detected between the XRD patterns of the sample subjected to a sole solutionizing and the one subjected to the full T6-sequence.

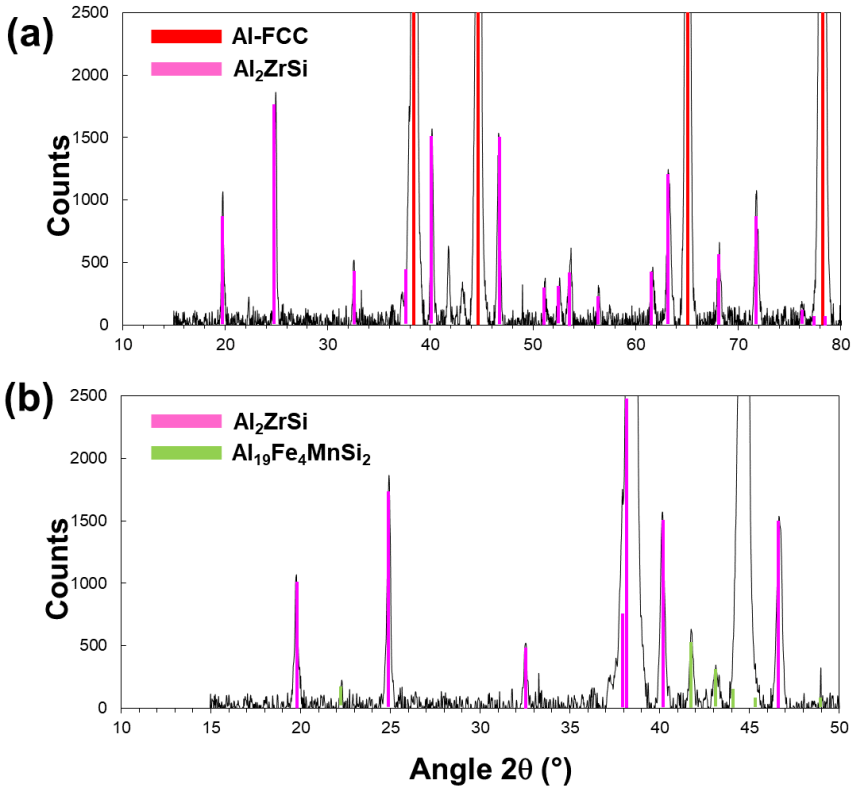

Figure 7. XRD pattern collected on a sample subjected to 550°C/30min. (a) in the (10°, 80°) angular range, the main diffraction peaks are indexed as FCC-Aluminium (a = 4.05 Å, red lines) and tetragonal Al_2ZrSi phase (Pearson symbol tI8 I4/mmm (139), a = b = 3.88 Å, and c = 8.98 Å, pink lines). (b) Enlarged views of the XRD patterns in the 10-50° range. The green lines can be indexed as a cubic structure with a large lattice parameter a = 12.60 Å, consistent with the $Al_{19}Fe_4MnSi_2$ (Pearson symbol cP168 Pm-3 (200)).

STEM images and EDXS maps of a TZ after solutionizing at 550°C/30 min are shown in **Figure 8**. Note that this region was not affected by recrystallization. Numerous intermetallic phases can be observed: the globular ones enriched in Fe, Mn, and Si (**Figure 8c, g, and e)** are thought to be the intermetallic $Al_{19}Fe_4MnSi_2$ phase detected in the XRD patterns. Zr and Si particles showing a needle-shaped morphology (**Figure 8e-f**) are rather associated with the Al_2ZrSi phase also identified on the XRD pattern. Interestingly, very few intermetallic particles are enriched in Mg after solutionizing 550°C/30 min and most of them appear to be oxides (see **Figure 8d** and **Figure 8i**). The selected area diffraction pattern shows the absence of the $L1_2$ signature of the nano precipitates (**Figure 8b**).

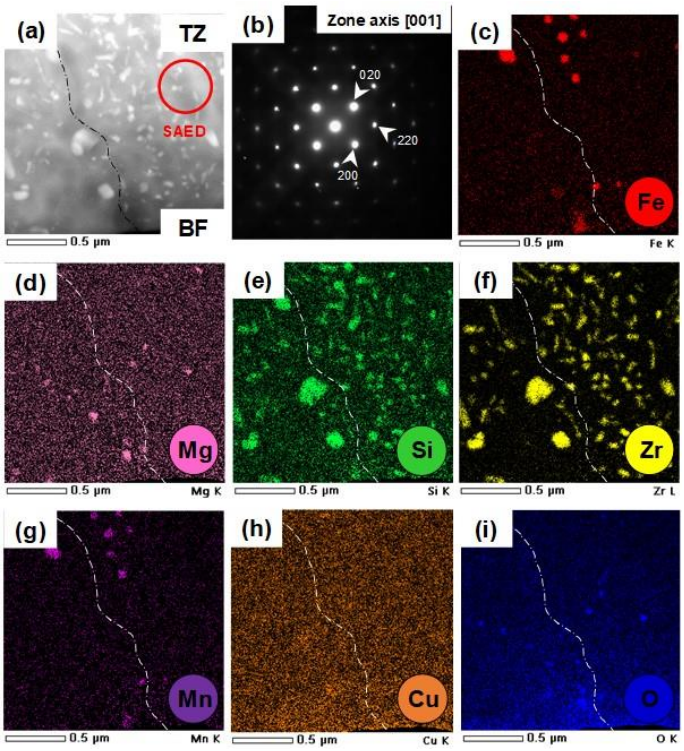

Figure 8. Overview of the microstructure after 550°C/30min. (a) STEM-BF image taken in the TZ. (b) Selected area electron diffraction (SAED) patterns from the region highlighted in red in (a). EDXS maps of the main solutes in the same region of interest: (c) Fe, (d) Mg, (e) Si, (f) Zr, (g) Mn, (h) Cu, and (i) O.

Samples subjected to the full T6-sequence were also examined in TEM, see **Figure 9**. The presence of β''-nano precipitates with a needle morphology can be seen on the TEM-BF image shown in **Figure 9** and is confirmed by the characteristic diffuse streaks on the selected area diffraction, see yellow arrows in **Figure 9b**. It means that the solutionizing at 550°C for 30 min was efficient in achieving a supersaturated solid solution in Mg and Si in the Zr-modified 6061 alloy that is decomposed during ageing at 180°C to precipitate the β''-phase that is known for years to strengthen the standard Al-Mg-Si alloys [42–44].

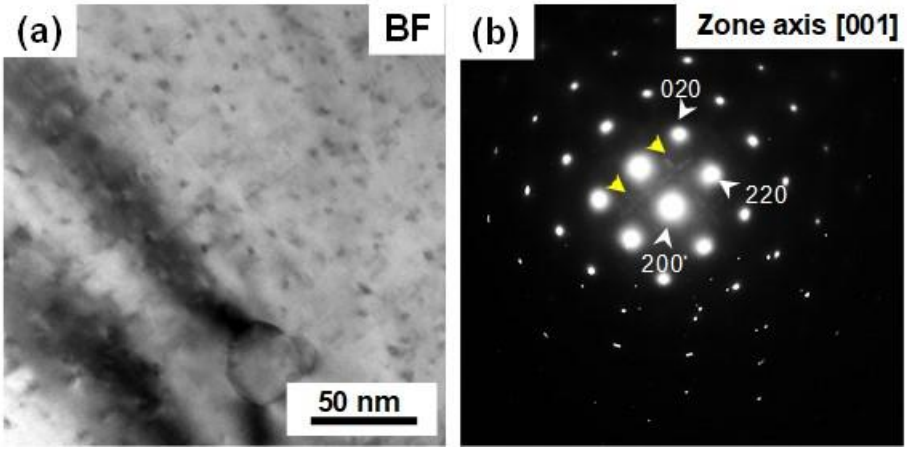

Figure 9. (a) STEM-BF image after 550°C/30min + Ageing at 180°C/4h. (b) Selected area electron diffraction showing the presence of β'' precipitates.

3.4.2. Direct ageing at 400°C

The first objective of direct ageing at 400°C on PBF-LB produced samples was to clarify if the high solid-liquid interface velocities and cooling rates typical of PBF-LB were sufficient to retain Zr in a supersaturated solid solution. Direct ageing at 400°C was thus done to evaluate the material strengthening through Al_3Zr-$L1_2$ precipitates. The evolutions of hardness and thermal conductivity were measured after direct ageing at 400°C on the Zr-modified 6061 alloy produced by PBF-LB, see **Figure 10a-b**. Similar measurements were carried out on a standard wrought 6061 alloy subjected to solutionizing followed by an annealing at 400°C, the results are also reported in **Figure 10a-b**. After direct ageing at 400°C, the Zr-modified 6061 alloy shows an increase of hardness over the first hour from 115 HV in the as-fabricated conditions to nearly 150 HV after 1h of ageing (**Figure 10a**). A peak is reached between 1 and 4h with a maximum hardness stable around 150 HV. For longer ageing treatments, overaged conditions are achieved since the hardness starts to decrease (about 120 HV after 24h at 400°C). While the hardness reaches a peak between 1 and 4 h, the thermal conductivity deduced from electrical conductivity measurements continuously increases from about 98 W/m.K in the as-fabricated conditions to nearly 168 W/m.K after 400°C/24h (**Figure 10b**). Annealing at 400°C of the standard cast and wrought 6061 alloy leads to a slight softening of the standard cast and wrought 6061 alloy with a hardness of 55 HV after solutionizing and 43 HV after 12h at 400°C (**Figure 10a**). The thermal conductivity remains almost constant and equal to about 185 W/m.K regardless of ageing time (**Figure 10b**).

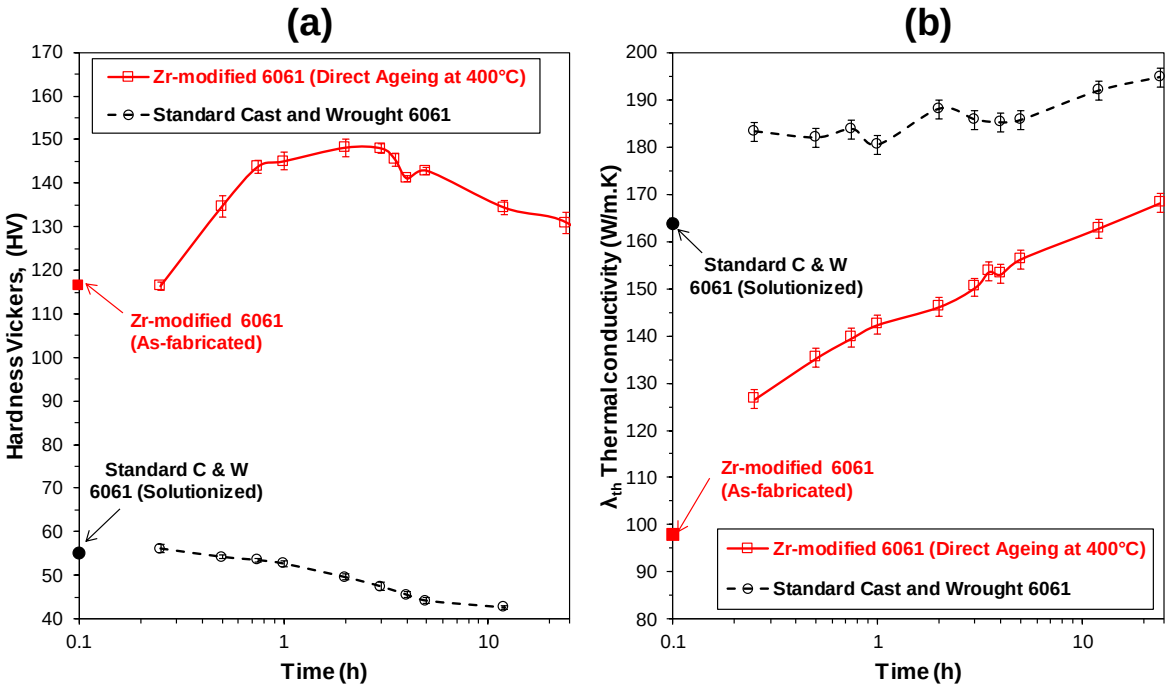

Figure 10. (a) Hardness and (b) thermal conductivity evolution with time after direct ageing at 400°C for the Zr-modified 6061 alloy. Results are also given for a standard cast and wrought 6061 alloy subjected to a solutionizing at 550°C followed by annealing at 400°C.

In order to understand how direct ageing at 400°C substantially improves both the hardness and thermal conductivity, we investigate the microstructural evolutions induced by such a treatment. As shown by the EBSD map in **Figure 11**, after direct ageing at 400°C/4 h, the grain structure remained unchanged compared to the as-fabricated conditions.

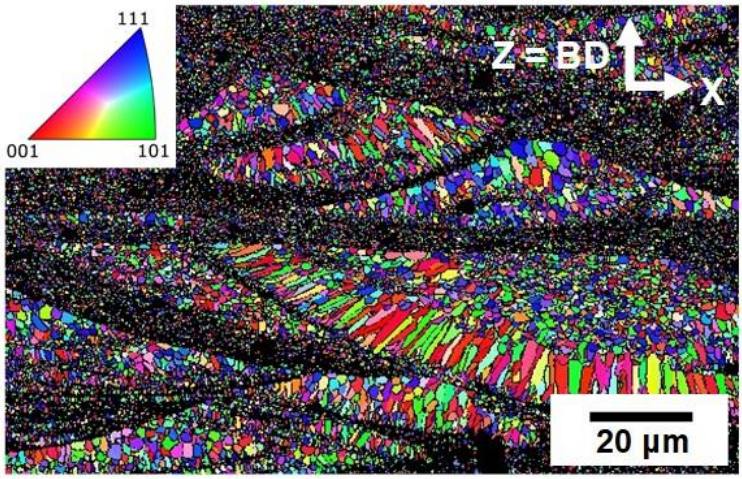

Figure 11. High-magnification EBSD-IPF map acquired a Zr-modified sample subjected to direct ageing 400°C/4 h (step size of 100 nm).

The XRD pattern shown in **Figure 12** after 400°C/4h reveals a few additional peaks in comparison with the XRD pattern of the as-fabricated sample shown in **Figure S 5**. Three intermetallic phases could be detected: Al_2ZrSi, Mg_2Si, and $Al_{16.8}Mn_{0.75}Fe_{3.25}Si_{2.2}$. Interestingly, the stable Mg_2Si phase was evidenced in the XRD pattern after direct ageing at 400°C/4 h but was not detected after solutionizing at 550°C/30 min suggesting that it was dissolved.

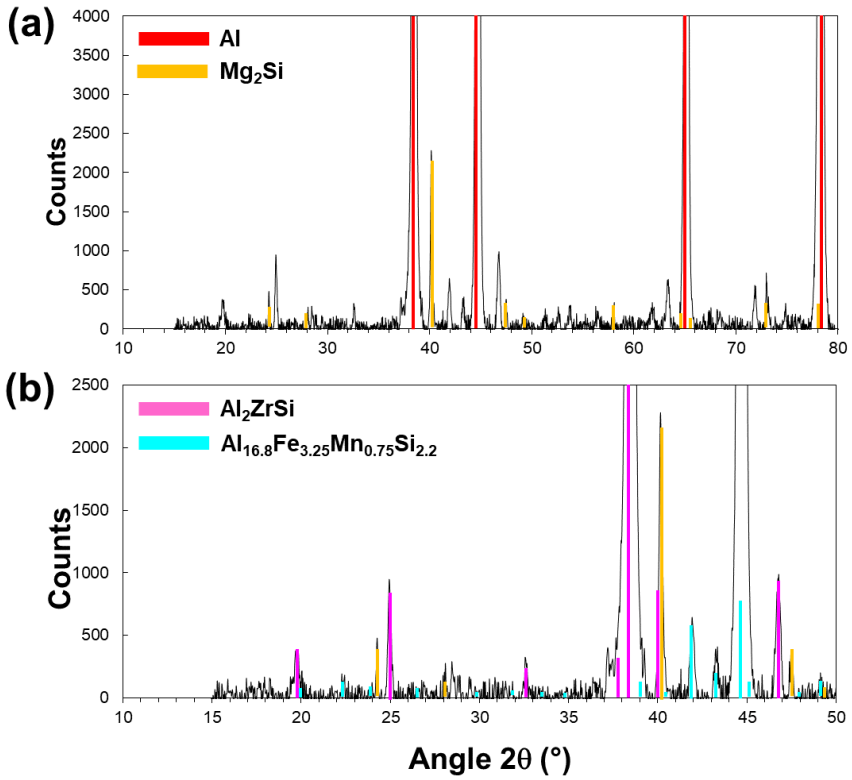

Figure 12. XRD patterns collected on a sample subjected to direct ageing at 400°C/4h: (a) in the (10°, 80°) angular range, the main diffraction peaks are indexed as FCC-Aluminium (a = 4.05 Å, red lines) and Mg_2Si cubic structure (Pearson symbol CF16, Fm-3m (225), a = 6.34910 Å, orange lines). (b) Enlarged views of the XRD patterns in the 10-50° range. The pink lines can be indexed as a tetragonal structure with lattice parameters a = b = 3.88 Å, and c = 8.98 Å, consistent with the Al_2ZrSi phase (Pearson symbol tI8, I4/mmm (139)). The light blue lines can be indexed as a cubic structure with a large lattice parameter a = 12.56 Å associated to the structure type phase $Al_{16.8}Mn_{0.75}Fe_{3.3}2Si_{2.2}$ (Pearson symbol cI168, I-3m (204)). The XRD indexing is based on the crystallographic information from the ICCD PDF4 + database. Though the exact composition might be different, the various phases will be referred to by the chemical formula from this XRD database.

At a finer scale, substantial evolutions have also been evidenced in the EZ and CZ at the micro and nanoscale based on TEM analyses. **Figure 13a** and **Figure 13b** give an overview of the microstructure respectively in the EZ and CZ and have to be respectively compared with **Figure 3a** and **Figure 3b** (at different scales) to better appreciate the differences induced by direct ageing at 400°C/4h at the microscale. In the EZ, we still observe the square-shaped precipitates corresponding to the primary Al_3Zr acting as a nucleating agent for the Al matrix (see black arrow in the STEM-BF image in **Figure 13a**), the latter being absent in the CZ as already observed in **Figure 3a**. After 400°C/4h, in addition to oxides enriched in Mg or Si, intermetallic particles can be seen in each zone. The Al_2ZrSi, Mg_2Si, and $Al_{16.8}Fe_{3.25}Mn_{0.75}Si_{2.2}$ intermetallic phases detected in the X-ray diffraction pattern of the sample 400°C/4h can be found in the EDXS maps shown in **Figure 13a** and **Figure 13b** based on the solute enrichment of the different intermetallic particles. Overall, these intermetallic particles are coarser than the ones observed in the as-fabricated conditions. Such microstructural evolutions cannot be invoked to account for the strengthening of the material induced by direct ageing at 400°C for 4h.

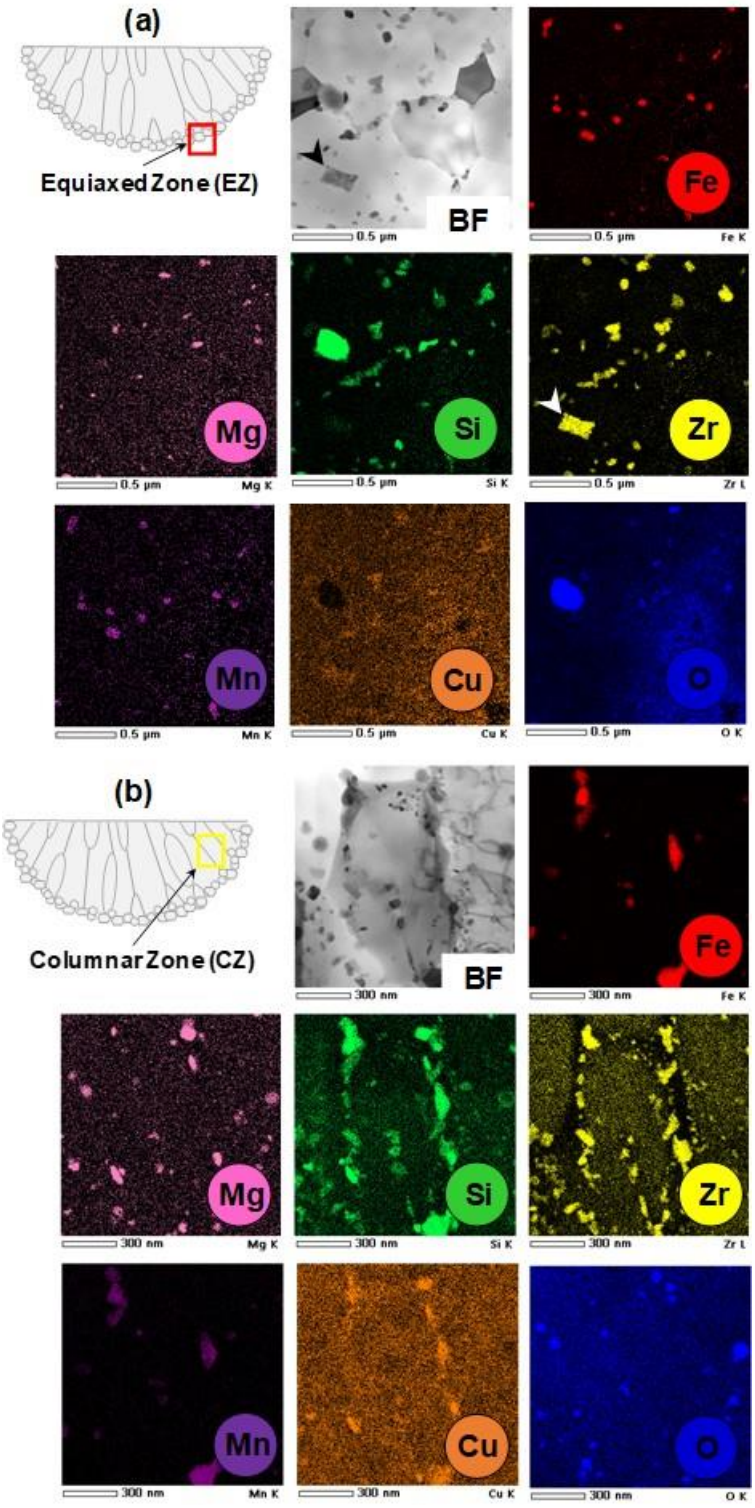

Figure 13. Overview of the microstructure after direct ageing at 400°C/4h revealed by STEM and EDXS mapping: (a) in the EZ and (b) in the CZ.

To investigate the presence of nano precipitates that could possibly explain the strengthening of the material, complementary TEM analyses were carried out in the EZ and CZ, see respectively **Figure 14a-b** and **Figure 14c-e**. Selected area electron diffraction (SAED) patterns ([001] zone axis) taken from the regions highlighted in red show the presence of a superstructure typical of an $L1_2$ coherent phase. Using dark-field imaging by selecting the [100] reflections, a high density of nano precipitates has been evidenced (**Figure 14e**).

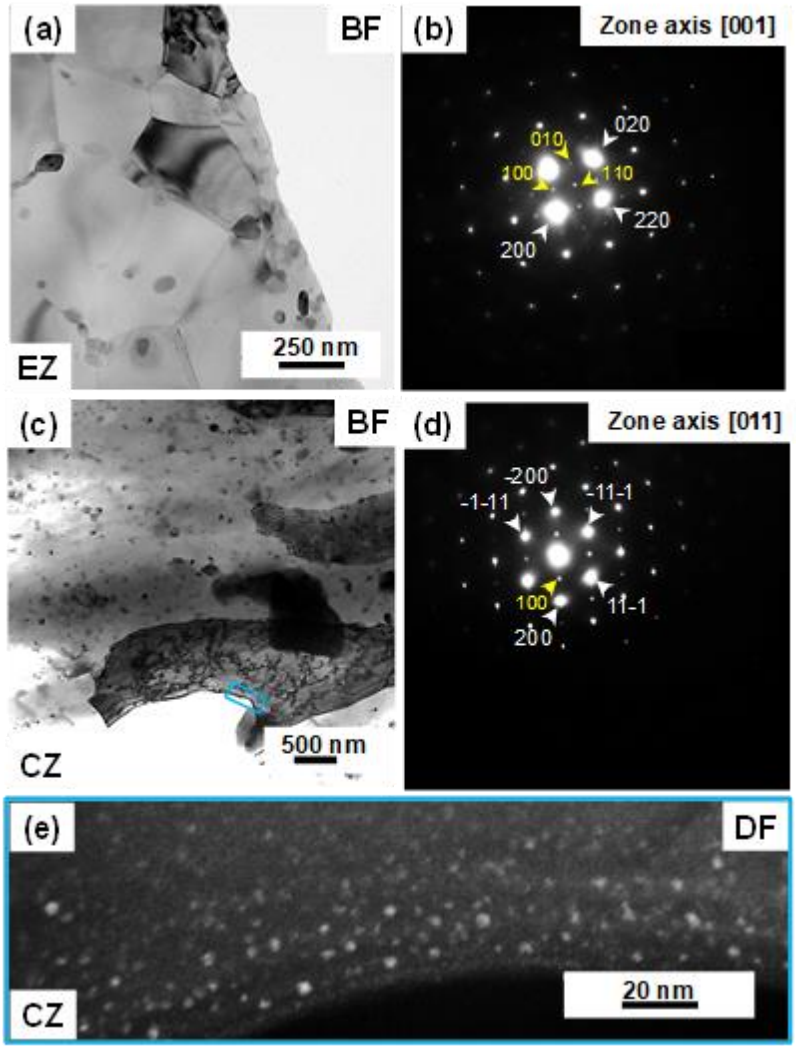

Figure 14. (a) and (c) TEM-BF image taken respectively in the EZ and CZ after direct ageing at 400°C/4h. (b) and (d) Selected area electron diffraction (SAED) patterns taken from the region shown in (a) and (c). (e) TEM-DF image of the region highlighted in blue in (c) ([100] reflections).

3.5. Tensile mechanical properties

The tensile mechanical response of the as-fabricated material as well as after various post-fabrication heat treatments were determined and are respectively given in **Figure 15a** and **Figure 15b**. As several tensile tests were performed for each condition, we noticed a good reproducibility between the different tests for a given condition, except for the ductility in the as-fabricated conditions, see **Figure 15a**.

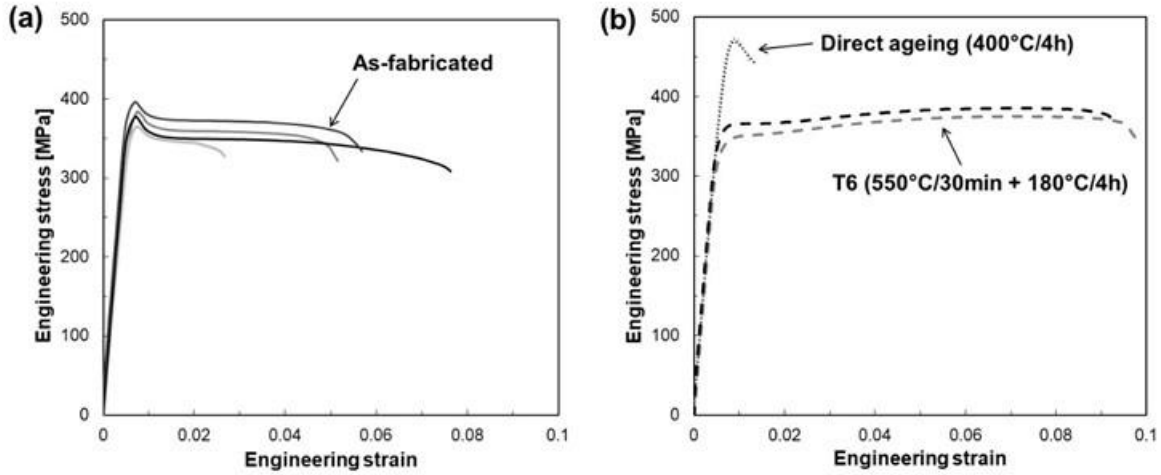

Figure 15. Tensile mechanical response: (a) in the as-fabricated conditions and (b) after post-fabrication heat treatments: direct ageing (400°C/4h) and T6 (550°C/30min + 180°C/4h).

According to the correlation between the pore content estimated by XCT and the ductility in the as-fabricated conditions (**Figure 16**), the dispersion of the elongation to failure in the as-fabricated conditions was explained by the variability of the pore volume fraction found in the different tensile specimens. This variability in the distribution of defects was attributed to thermo-optic effects as suggested by Bonhof et al. [45]. Instability of the beam focusing position may indeed occur during the section's edification, especially for large areas. Minor but randomized defects are thus generated in the samples leading, to a heterogeneous distribution of pores as illustrated in the different samples characterized using X-ray tomography, see **Figure 16**.

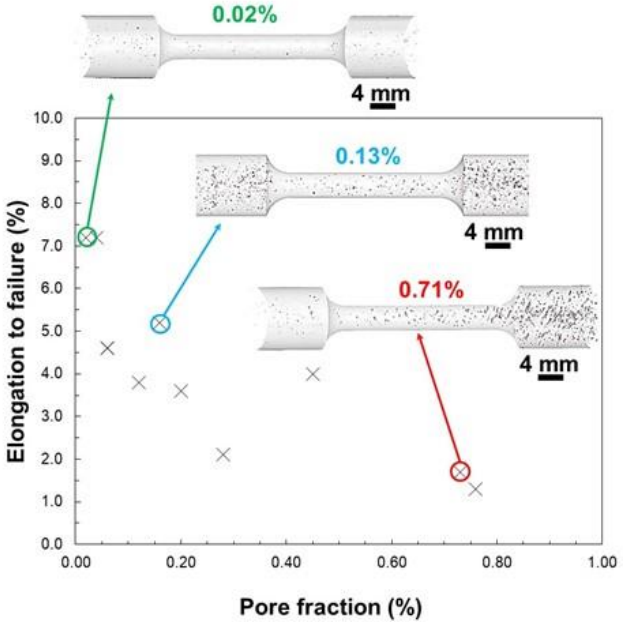

Figure 16. Evolution of the ductility as a function of pore fraction for samples tested in the as-fabricated conditions. Pore fraction was measured by XCT in the gauge length of the tensile specimens.

The mechanical properties extracted from the tensile responses are summarized in **Table 4**. In the as-fabricated conditions, the Zr-modified alloy shows a yield strength that is nearly 100 MPa higher than the one of a standard cast and wrought 6061 alloy (fabricated by the traditional cast and wrought processing route) in its T6 conditions but this goes along with a loss of ductility (about 5% for the Zr-modified alloy vs. more than 15% for the standard cast and wrought 6061-T6 alloy [46]). Interestingly, a standard T6 treatment applied to the Zr-modified alloy does not really change its yield strength in comparison with its as-fabricated counterpart (370 vs. 350 MPa) but the ductility is almost doubled (4.5 vs. 8.3%). The Zr-modified 6061 alloy subjected to a standard T6-sequence outperforms the standard cast and wrought 6061-T6 in terms of yield strength. After direct ageing at 400°C/4h, the Zr-modified alloy is further strengthened with a yield strength greater than 450 MPa but becomes brittle with an elongation to failure < 1%.

	Yield Strength, $\sigma_{e,0.2\%}$ (MPa)	**Ultimate tensile, σ_{UTS} strength (MPa)**	**Elongation to failure A (%)**
Zr-modified 6061 Alloy (Zr = 2.3 wt.%) This work			
As-fabricated	370 ± 18	372 ± 20	4.5 ± 2
550°C/30min + 180°C/4h	350 ± 10	382 ± 5	8.3 ± 1
Direct aged 400°C/4h	460 ± 15	470 ± 5	0.4 ± 0.3
Standard cast and wrought 6061 Alloy			
6061-T6 (550°C/2h + 180°C/4h) ASM Standard [46]	276	310	17
6061-T4 (550°C/2h + naturally aged) ASM Standard [47]	145	240	22

Table 4. Summary of the mechanical properties of the Zr-modified 6061 alloy in the as-fabricated conditions and after post-fabrication heat treatments: direct ageing (400°C/4h) and T6 (550°C/30min + 180°C/4h). Values are also given for a standard cast and wrought 6061 alloy subjected to a T6 or T4 heat treatment.

4. Discussion

Before discussing the microstructure-property relationship in the different microstructures produced in this work, we would like to highlight that the Zr-modified 6061 alloy shows good processability as no hot cracks were detected in the as-fabricated samples. Furthermore, since the porosity content was measured to be lower than 1%, this should not significantly impact the conductivity measurements. In addition, we also estimated the diffusion lengths of the main solutes, namely Si, Mg, and Zr, after 4h at 400°C and 180°C, see **Table 5**. Such calculations will be further used to discuss some aspects of the microstructure-property relationships in the different microstructures investigated in this work.

	D_0 (m²/s)	Q (kJ/mol)	Reference	L, Diffusion length (µm)	
				400°C/4h	180°C/4h
Si	$1.38\ 10^{-5}$	117.6	[48]	29.8	0.181
Mg	$1.49\ 10^{-5}$	120.5	[48]	23.9	0.128
Zr	$7.28\ 10^{-2}$	242.0	[49]	0.032	$8.8\ 10^{-7}$

Table 5. Estimation of the diffusion length of various solutes (Si, Mg and Zr) in FCC-Al after 400°C/4h or 180°C/4h using $L = \sqrt{\langle 6Dt \rangle}$ *with* $D = D_0 \exp(-Q/RT)$.

4.1. Microstructure-property relationships in the as-fabricated material.

The as-fabricated material shows a relatively high yield strength, beyond 350 MPa in comparison to about 270-280 MPa in a standard cast and wrought 6061-T6, see **Table 4.** This value is also substantially higher than the 210 MPa reported in [27] and the 241 MPa reported in [17] for as-fabricated Zr-modified 6061 alloys with respectively 1.0 and 1.2 wt.% Zr. Such a high yield strength can be accounted for by various strengthening contributions. The objective hereafter is not necessarily to provide systematically quantitative estimates of the various contributions: (i) Hall-Petch due to grain size, (ii) solid solution strengthening, (iii) residual stresses/dislocations, and (iv) precipitation strengthening as suggested in [27] and [17]. We will rather attempt to estimate which of those contributions are predominant because providing estimates of the various contributions often depends on many parameters that are not necessarily properly measured or that show a non-negligible degree of variability.

(i) The classical Hall-Petch relationship $\Delta\sigma_{GB} = k_y d^{-0,5}$ with k_y the Hall-Petch slope and d the average grain size, was adapted to the dual grain structure observed in our as-fabricated composite-like microstructure using a rule of mixture:

$$\Delta\sigma_{GB} = V_{EZ} k_y d_{EZ}^{-0,5} + V_{CZ} k_y d_{CZ}^{-0,5}$$

with V_{EZ} and V_{CZ} respectively the volume fraction of the EZ and CZ, and d_{EZ} and d_{CZ} respectively the average grain size in the EZ and CZ. Taking k_y = 0.14 MPa.m$^{1/2}$ [50], V_{EZ} = 0.2, d_{EZ} = 600 nm, and V_{CZ} = 0.8 d_{CZ} = 5 µm, the grain boundary strengthening contribution was thus estimated to be $\Delta\sigma_{GB}$ = 180 MPa. This should be compared to a wrought 6061 alloy with grains of several hundreds of microns where the Hall-Petch contribution will be below 10 MPa. Interestingly, the grain boundary strengthening was found to be about only 64 MPa [17]. We think that this has to do with the k_y parameter used in their study (0.06 MPa.m$^{1/2}$) and the overall Zr content in their 6061 alloy which was half the one of the alloy investigated in this work. The latter likely contributes to increasing the proportion of fine equiaxed grains.

(ii) Solid solution strengthening $\Delta\sigma_{SS}$ is also expected to contribute to the strength in the as-fabricated conditions as we believe that a substantial amount of solutes could be retained in the supersaturated

solid solution. This is supported by our electrical and thermal conductivities measurements as it is known that such properties are drastically affected by the presence of atoms in solid solutions in metals and alloys [39]. As an upper boundary for the solid solution strengthening contribution, we can consider the case where all of the Zr, Mg, and Si solutes are trapped in the solid solution. Using Figure 16b of [51], the solid solution strengthening of the as-fabricated material should be below few $\Delta\sigma_{SS}$ < 50 MPa. Indeed, the actual solid solution is expected to be much lower since some solutes, particularly the fast diffuser Mg and Si, will be part of the intermetallic particles. This is in agreement with [17] where it was concluded that the solid solution strengthening contribution represents a minor contribution.

(iii) Residual stresses due to high cooling rates and that are known to generate dislocations in microstructures inherited from PBF-LB are also thought to contribute to the yield strength of the as-fabricated material. However, applying a stress-relief treatment performed at 300°C/4h only reduces the hardness from 116 HV to 110 HV showing that this contribution cannot be invoked to explain the high yield strength of the as-fabricated material.

(iv) Regarding a possible strengthening by Al_3Zr-$L1_2$ precipitates, given the slow diffusivity of Zr in Al, such precipitation would require a high temperature (nearly 400°C) exposition for at least some minutes, something that does not happen in PBF-LB given the very high cooling rates. Potentially, small regions located in the heat-affected zone of the various molten pools can be heated at temperatures close to 400°C but for such a short period of time that it is thought to be not long enough to trigger clustering that would be precursors of Al_3Zr-$L1_2$ precipitates (**Table 5**).

However, it is known for years that Al alloys from the 6XXX series can be naturally aged [52–55] and this aspect was not considered in previous studies, see e.g. [17,27]. To evaluate how natural ageing could contribute to the yield strength in our case, a few as-fabricated samples were kept at -20°C right after the PBF-LB fabrication, and their hardness (115 ± 2 HV) was then compared to the one measured on as-fabricated samples stored at room temperatures for several months (123 ± 3 HV). We did detect a slight increase but at a first sight we concluded that natural ageing could not have a significant contribution to the very high yield strength of the as-fabricated material. Indeed, here, we rather think that a non-negligible contribution to the high yield strength of the as-fabricated material results from in situ clustering of Mg and Si during the intrinsic heat treatment experienced by the material during PBF-LB. This is in agreement with the recent work of Lefebvre et al. [56] that revealed by atom probe tomography the presence of clusters in the as-fabricated microstructure of an AlSi10Mg alloy processed by PBF-LB. One has to keep in mind that samples produced by PBF-LB have a complex thermal history due to thermal cycling, this is why we described this phenomenon as in situ clustering during the intrinsic heat treatment. The latter idea was supported by the comparison of the DSC signal of an as-fabricated Zr-modified sample with its solutionized counterpart (as-fabricated sample subjected to solutionizing at 550°/30 min), see **Figure 17**. Interestingly, an endothermal peak near 140°C was detected in the as-fabricated material but was absent in the solutionized one. Such an endothermal peak was attributed to the dissolution of clusters as suggested in [54]. Such clusters have been found to strengthen the material, see e.g. [54,55]. For example, one week of natural ageing in the 6016 alloy leads to an increase of hardness from about 40 HV to nearly 65 HV, see [54]. Thus, we believe that in situ clustering occurring during thermal cycling in PBF-LB could greatly contribute to the 370 MPa in yield strength of the as-fabricated material.

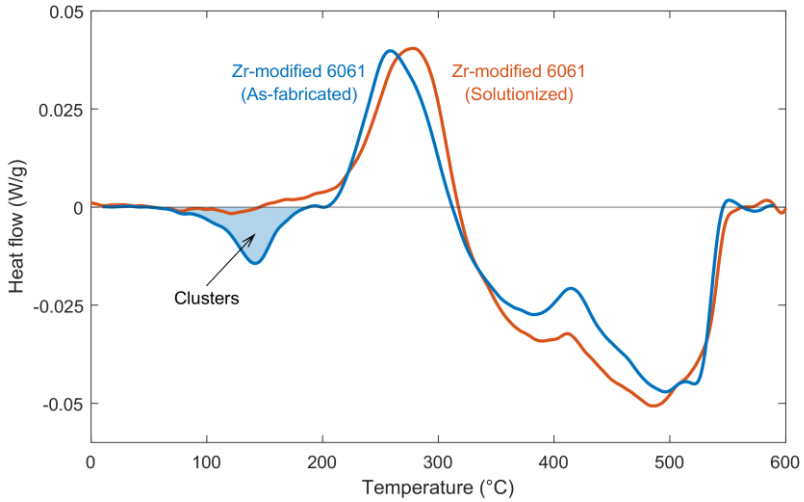

Figure 17. Comparison of the DSC signal of a Zr-modified as-fabricated sample (in blue) with the one of its solutionized counterpart (in orange: as-fabricated sample subjected to solutionizing at 550°/30min). Heating rate 20 K/min.

To summarize, in the as-fabricated condition, grain boundary strengthening is the predominant strengthening mechanism as it contributes to nearly half the yield strength. The second important strengthening contribution is thought to be the one caused by the clusters that form during the intrinsic heat treatment experienced by the material during L-PBF. The other strengthening mechanisms are thought to bring minor contributions to the overall yield strength.

4.2. Microstructure and property evolutions induced by a T6-sequence

Direct ageing at 180°C did not turn out to be a relevant option to achieve a compromise between strength and conductivity. Hardness only slightly increases from 116 HV in the as-fabricated sample vs. 120 HV after direct ageing at 180°C/4h. The thermal conductivity has only slightly increased from 98 to 101 W/m.K indicating that ageing for 4h at 180°C was not enough to induce the decomposition of the Zr-rich supersaturated solid solution. The lack of precipitation strengthening, which at this temperature can only originate from Mg and Si through the formation of β'', can be explained by the much smaller grain size compared to conventional wrought alloys. The diffusion length of Mg and Si at 180°C allows them to explore the whole grain so that the heterogeneous nucleation and coarsening of more stable phases at grain boundaries is more likely (i.e. faster) than homogeneous nucleation of a metastable phase inside the grains, see **Table 5**. On the other hand, at this temperature, Zr is not mobile and stays in solid solution, yielding a low thermal conductivity.

A first pathway to achieve a good compromise between strength and conductivity is given by subjecting the as-fabricated material to a T6-sequence, the yield strength (350 ± 10 MPa) being very close to that of the as-fabricated material (370 ± 18 MPa) while the conductivity reaches 170 W/m.K , a value much closer to the one measured on a standard cast and wrought 6061-T6 (173 W/m.K) compared to that measured in the as-fabricated material (98 W/m.K). Here, it should be emphasized that in [27] and [17], an increase in yield strength between the as-fabricated material and the one subjected to T6 heat treatment was found (210 vs. 300 MPa [27], 241 vs. 289 MPa [17] whereas in the present study, we measured a slight decrease, by about 20 MPa. Once again this is certainly due to the higher Zr content in the material investigated here (2.3 vs. 1.0 wt.% in [27] and 1.2 wt.% in [17]) suggesting that there is room to further explore the property space by playing with the Zr-content in modified alloys.

Interestingly, both the hardness and yield strength of the Zr-modified alloy investigated in this work show similar values in the as-fabricated conditions and subsequently to a T6 sequence. However, the

underlying strengthening mechanisms are thought to differ strongly. To better appreciate the evolutions of both hardness and thermal conductivity during a T6 sequence, samples subjected to solutionizing heat treatment at 550°C/30min only were characterized, see **Figure 6** and **Figure 8**. Solutionizing led to a significant drop in hardness: from 116 HV in the as-fabricated material to 85 HV after solutionizing. This is thought to be primarily the consequence of a change in grain structure with the presence of a partially recrystallized microstructure, with the largest grains exceeding several hundreds of microns as illustrated in **Figure 6**. Considering now that 40% of the microstructure consists of fine equiaxed grains (V_{EZ} = 0.4) with a size similar in comparison to the as-fabricated material (d_{EZ} = 600 nm) and the other 60% (V_{REC} = 0.6) are associated to large recrystallized grains with an average size d_{REC} ≈ 100 µm, the grain boundary strengthening estimated as above is $\Delta\sigma_{GB}$ ≈ 100 MPa. Compared to $\Delta\sigma_{GB}$ ≈ 180 MPa estimated for the as-fabricated material, it means that grain boundary strengthening has been nearly divided by a factor of 2. This partial recrystallization certainly goes along with a reduction of the residual stresses inherited from the process and the possible annihilation of some dislocations present in the as-fabricated material that can further slightly contribute to decreasing the yield strength after solutionizing. The dissolution of the clusters evidenced by DSC in the as-fabricated material is also expected to contribute to the material softening after solutionizing. Although the solution heat treatment has likely increased the amount of Mg and Si in the solid solution, the thermal conductivity has been greatly improved: from 98 W/m.K in the as-fabricated material to 160 W/m.K after 550°C for 30 minutes, see **Table 3**. This can be attributed to the depletion of Zr from the solid solution because Zr was consumed by the formation of coarse Zr-rich precipitates as shown in **Figure 8**. Indeed, if such precipitation had not occurred, because of the Zr present in solid solution, the thermal conductivity would not have been lower. This is a confirmation that the effect of the solid solution on the thermal conductivity is dominated by Zr [40,57].

After solutionizing at 550°C/30 min, the material gets strengthened during ageing at 180°C/4h with a hardness close to 125 HV, see **Table 3**. This increase in hardness from 85 HV to nearly 125 HV is attributed to precipitation of the well-known β'' metastable phase [44], which was evidenced based on TEM analyses in **Figure 9**. However, for the same reason as for the direct ageing at 180°C in the region consisting of small equiaxed grains, β'' precipitates are not likely to be dominant, so they probably only strengthen the grains that underwent recrystallization. This precipitation goes along with an additional increase of the thermal conductivity about 170 W/m.K vs. 160 W/m.K after solutionizing, still slightly lower than that of a standard T6-6061 (173 W/m.K).

To summarize, applying a T6 treatment is a good option to achieve a coupled strength-conductivity trade-off in the Zr-modified 6061 alloy. In this case, the role of the Zr-addition is essentially to make the alloy processable by refining the grain size to increase its hot cracking resistance. Zr does not play a key role regarding the yield strength while it has a major effect on the thermal conductivity.

4.3. Microstructure and property evolution induced by direct ageing at 400°C/4h

Direct ageing at 400°C/4h seems another good option to achieve a good compromise between strength (yield strength of about 450 MPa) and conductivity (above 150 W/m.K). Indeed, the hardness increases substantially from 116 HV in the as-fabricated conditions to nearly 150 HV after direct ageing at 400°C for 4h. Both the standard cast and wrought 6061-T6 and the Zr-modified 6061 subjected to a T6 sequence are outperformed in terms of mechanical strength (yield strength beyond 450 MPa vs. respectively 270 MPa and 300 MPa for a standard cast and wrought 6061-T6 [46] and Zr-modified 6061-T6 with 1.0 wt.% Zr [27]) but this goes along with a drastic drop in ductility. The directly aged material becomes very brittle: elongation to failure < 1% vs more than 15% for a standard cast and wrought 6061-T6 alloy and more than 8% for the Zr-modified 6061-T6, see **Table 4**. Regarding the thermal conductivity, the performance of a standard cast and wrought 6061-T6 (about 173 W/m.K) has not yet been reached (149 W/m.K) although it has increased in comparison with the as-fabricated material.

This improvement in thermal conductivity can be explained by a significant solute redistribution after ageing at 400°C for 4h, in particular for Zr through a dual effect. First, we evidenced the presence of the Al_2ZrSi phase by XRD (**Figure 12**) which was further confirmed in the EDXS maps with coarse particles enriched in Si and Zr (**Figure 13**). This phase was not detected in the as-fabricated conditions. Second, we evidenced based on TEM analyses the presence of Al_3Zr $L1_2$ precipitates, see **Figure 14**. This dual effect led to a reduction of the Zr content in the supersaturated solid solution and thus to increased conductivity.

As discussed for the other microstructures, it is of interest to further examine the different strengthening mechanisms after direct ageing at 400°C for 4h. On the grain scale, no significant changes were found, see the comparison between **Figure 1b** and **Figure 11**. This contrasts with the important microstructural evolution evidenced in **Figure 6** with the presence of large recrystallized grains. This means that the grain boundary strengthening contribution is expected to be as high as in the as-fabricated material ($\Delta\sigma_{GB}$ ≈ 180 MPa). Here, the clusters suspected of strengthening the material in the as-fabricated material have been dissolved and the strengthening by the solid solution can be neglected because, after 400°C/4h, coarse stable Mg_2Si are expected to form as confirmed by the XRD pattern shown in **Figure 12**. In addition, the Al_3Zr $L1_2$ precipitation evidenced based on TEM analyses (**Figure 14**), consumes most of the Zr initially retained in the supersaturated solid solution ($\Delta\sigma_{SS}$ ≈ 0 MPa). The contribution of residual stresses to the overall yield strength can also be neglected because stress-relief is likely to occur at such a high temperature in Al alloys. Thus, the hardness increase upon direct ageing at 400°C/4h is mainly attributed to the high density of nanoscale spherical Al_3Zr $L1_2$ precipitates as evidenced based on TEM analyses, see **Figure 14** and in agreement with [17,27].

In summary, in the case of direct ageing at 400°C/4h, Zr not only helps to make the alloy processable by PBF-LB but also contributes to significantly strengthening the material via the nanoprecipitation of spherical Al_3Zr $L1_2$.

5. Conclusions

The introduction of 2.3 wt.% of Zr in the composition of the heritage 6061 alloy makes this alloy processable by PBF-LB (suppression of hot cracks) thanks to grain refinement, in agreement with previous publications. It was shown that the addition of such a large amount of Zr affects the as-fabricated microstructure at all scales.

Under its as-fabricated conditions, the yield strength of the Zr-modified 6061 alloy (370 MPa) produced in this work outperforms that of the standard cast and wrought 6061 alloy subjected to a T6 sequence (260 MPa). However, the thermal conductivity of the Zr-modified 6061 alloy (nearly 100 W/m.K) is drastically reduced compred to that of the heritage 6061 alloy under its T6 conditions (173 W/m.K). The high yield strength of the as-fabricated material results mainly from grain boundary strengthening and from the contribution of Mg/Si-rich clusters that are thought to form during the intrinsic heat treatment the material experienced during L-PBF. The other strengthening mechanisms only brought a minor contribution to the overall yield strength. The low thermal conductivity was attributed to the Zr retained in solid solution in the as-fabricated microstructure.

To achieve a good compromise between yield strength and thermal conductivity, two post-fabrication heat treatment sequences have been designed. In both cases, the strength is mainly caused by precipitation strengthening that is combined with a depletion of the solid solution that is also beneficial to electrical and thermal conductivities.

- A standard T6 sequence with a shorter solutionizing time (550°C/30 min) was shown to be a good option since the yield strength was still higher (350 MPa) than the heritage T6-6061 alloy (260 MPa) and the thermal conductivity was as good as the one of the heritage alloy subjected to a T6 sequence (about 170 W/m.K). Interestingly, after a T6 sequence, the yield strength of the Zr-modified 6061 was not significantly affected. However, the underlying strengthening mechanisms have changed since grain boundary strengthening is no longer the main contribution. The strengthening brought by the β'' precipitates becomes the predominant mechanism. The thermal conductivity nearly equals the one of the heritage T6-6061 alloy because the solid solution is depleted in Zr (Zr-rich phases have precipitated during solutionizing at 550°C) and in Mg and Si (precipitation of the β'' phase).
- After direct ageing at 400°C/4h, the yield strength reaches 460 MPa (nearly 100 MPa higher than the yield strength of the as-fabricated material) and the thermal conductivity is improved (about 150 W/m.K) but does not equal the one of the heritage T6-6061 alloy. In this case, both grain boundary strengthening and precipitation strengthening of the nanosized Al_3Zr $L1_2$ have been identified as the predominant mechanisms. The improvement in thermal conductivity is caused by the decomposition of the solid solution, which becomes depleted in Zr.

As a final remark, we noticed that the yield strength of the as-fabricated material as well as after the various heat treatments were systematically higher than the ones reported for similar alloys but containing only 1-1.2 wt.% Zr, see e.g. [17,27]. This suggests that adjusting the Zr content in Zr-modified Al-alloys should also be considered an interesting pathway to optimize the mechanical properties.

Acknowledgements

This work was supported by the THALES Company via the ANRT 2018/1549 funding. This work has also benefited from the characterization equipements of Grenoble INP – CMTC platform supported by the Center of Excellence of Multifunctional Architectured Materials "CEMAM" n°AN-10-LABX-44-01 funded by the Investments for the Future program.

Data availability

The raw/processed data required to reproduce these findings cannot be shared at this time as the data also forms part of an ongoing study.

References

[1] C. Zhang, S. Wang, J. Li, Y. Zhu, T. Peng, H. Yang, Additive manufacturing of products with functional fluid channels: A review, Additive Manufacturing. 36 (2020) 101490. https://doi.org/10.1016/j.addma.2020.101490.

[2] A. Niel, C. Bordreuil, F. Deschaux-Beaume, G. Fras, Modelling hot cracking in 6061 aluminium alloy weld metal with microstructure based criterion, Science and Technology of Welding and Joining. 18 (2013) 154–160. https://doi.org/10.1179/1362171812Y.0000000072.

[3] K. Prasad Rao, N. Ramanaiah, N. Viswanathan, Partially melted zone cracking in AA6061 welds, Materials & Design. 29 (2008) 179–186. https://doi.org/10.1016/j.matdes.2006.10.022.

[4] ISO/ASTM 5900:2021, Additive manufacturing — General principles — Fundamentals and vocabulary, (2021). https://www.iso.org/standard/74514.html.

[5] A. Sonawane, G. Roux, J.-J. Blandin, A. Despres, G. Martin, Cracking mechanism and its sensitivity to processing conditions during laser powder bed fusion of a structural aluminum alloy, Materialia. 15 (2021) 100976. https://doi.org/10.1016/j.mtla.2020.100976.

[6] N. Kouraytem, P.-J. Chiang, R. Jiang, C. Kantzos, J. Pauza, R. Cunningham, Z. Wu, G. Tang, N. Parab, C. Zhao, K. Fezzaa, T. Sun, A.D. Rollett, Solidification crack propagation and morphology dependence on processing parameters in AA6061 from ultra-high-speed x-ray visualization, Additive Manufacturing. 42 (2021) 101959. https://doi.org/10.1016/j.addma.2021.101959.

[7] S.Z. Uddin, L.E. Murr, C.A. Terrazas, P. Morton, D.A. Roberson, R.B. Wicker, E. Paso, Processing and characterization of crack-free aluminum 6061 using high- temperature heating in laser powder bed fusion additive manufacturing, Additive Manufacturing. 22 (2018) 405–415. https://doi.org/10.1016/j.addma.2018.05.047.

[8] Q. Tan, Y. Yin, A. Prasad, G. Li, Q. Zhu, D.H. StJohn, M.-X. Zhang, Demonstrating the roles of solute and nucleant in grain refinement of additively manufactured aluminium alloys, Additive Manufacturing. 49 (2022) 102516. https://doi.org/10.1016/j.addma.2021.102516.

[9] X.P. Li, G. Ji, Z. Chen, A. Addad, Y. Wu, H.W. Wang, J. Vleugels, J. Van Humbeeck, J.P. Kruth, Selective laser melting of nano-TiB2 decorated AlSi10Mg alloy with high fracture strength and ductility, Acta Materialia. 129 (2017) 183–193. https://doi.org/10.1016/j.actamat.2017.02.062.

[10] Y.K. Xiao, Z.Y. Bian, Y. Wu, G. Ji, Y.Q. Li, M.J. Li, Q. Lian, Z. Chen, A. Addad, H.W. Wang, Effect of nano-TiB2 particles on the anisotropy in an AlSi10Mg alloy processed by selective laser melting, Journal of Alloys and Compounds. 798 (2019) 644–655. https://doi.org/10.1016/j.jallcom.2019.05.279.

[11] J.H. Martin, B.D. Yahata, J.M. Hundley, J.A. Mayer, T.A. Schaedler, T.M. Pollock, 3D printing of high-strength aluminium alloys, Nature Publishing Group. 549 (2017) 365–369. https://doi.org/10.1038/nature23894.

[12] C. Galera-Rueda, M.L. Montero-Sistiaga, K. Vanmeensel, M. Godino-Martínez, J. Llorca, M.T. Pérez-Prado, Icosahedral quasicrystal-enhanced nucleation in Al alloys fabricated by selective laser melting, Additive Manufacturing. 44 (2021) 102053. https://doi.org/10.1016/j.addma.2021.102053.
[13] M. Opprecht, J. Garandet, G. Roux, C. Flament, M. Soulier, A solution to the hot cracking problem for aluminium alloys manufactured by laser beam melting, Acta Materialia. 197 (2020) 40–53. https://doi.org/10.1016/j.actamat.2020.07.015.
[14] M. Opprecht, J.-P. Garandet, G. Roux, C. Flament, An understanding of duplex microstructures encountered during high strength aluminium alloy laser beam melting processing, Acta Materialia. 215 (2021) 117024. https://doi.org/10.1016/j.actamat.2021.117024.
[15] J.R. Croteau, S. Grif, M.D. Rossell, C. Leinenbach, C. Kenel, V. Jansen, D.N. Seidman, D.C. Dunand, N.Q. Vo, Microstructure and mechanical properties of Al-Mg-Zr alloys processed by selective laser melting, 153 (2018) 35–44. https://doi.org/10.1016/j.actamat.2018.04.053.
[16] Q. Li, G. Li, X. Lin, D. Zhu, J. Jiang, S. Shi, F. Liu, W. Huang, K. Vanmeensel, Development of a high strength Zr/Sc/Hf-modified Al-Mn-Mg alloy using Laser Powder Bed Fusion: Design of a heterogeneous microstructure incorporating synergistic multiple strengthening mechanisms, Additive Manufacturing. 57 (2022) 102967. https://doi.org/10.1016/j.addma.2022.102967.
[17] M. Opprecht, G. Roux, J.-P. Garandet, C. Flament, A Study of the Mechanical Properties of Al6061-Zr1,2 Alloy Processed by Laser Beam Melting, J. of Materi Eng and Perform. (2022). https://doi.org/10.1007/s11665-022-07218-0.
[18] Q. Jia, P. Rometsch, P. Kürnsteiner, Q. Chao, A. Huang, Selective laser melting of a high strength Al-Mn-Sc alloy : Alloy design and strengthening mechanisms, Acta Materialia. 171 (2019) 108–118. https://doi.org/10.1016/j.actamat.2019.04.014.
[19] K.V. Yang, Y. Shi, F. Palm, X. Wu, P. Rometsch, Columnar to equiaxed transition in Al-Mg(-Sc)-Zr alloys produced by selective laser melting, Scripta Materialia. 145 (2018) 113–117. https://doi.org/10.1016/j.scriptamat.2017.10.021.
[20] M. Buttard, B. Chehab, R. Shahani, F. Robaut, G. Renou, C. Tassin, E. Rauch, P. Donnadieu, A. Deschamps, J.-J. Blandin, G. Martin, Multi-scale microstuctural investigation of a new Al-Mn-Ni-Cu-Zr aluminium alloy processed by laser powder bed fusion, Materialia. 18 (2021) 101160. https://doi.org/10.1016/j.mtla.2021.101160.
[21] C. Pauzon, A novel laser powder bed fusion Al-Fe-Zr alloy for superior strength-conductivity trade-off, Scripta Materialia. (2022) 7.
[22] Q. Jia, F. Zhang, P. Rometsch, J. Li, J. Mata, M. Weyland, L. Bourgeois, M. Sui, X. Wu, Precipitation kinetics, microstructure evolution and mechanical behavior of a developed Al–Mn–Sc alloy fabricated by selective laser melting, Acta Materialia. 193 (2020) 239–251. https://doi.org/10.1016/j.actamat.2020.04.015.
[23] S. Griffiths, M.D. Rossell, J. Croteau, N.Q. Vo, D.C. Dunand, C. Leinenbach, Effect of laser rescanning on the grain microstructure of a selective laser melted Al-Mg-Zr alloy, Materials Characterization. 143 (2018) 34–42. https://doi.org/10.1016/j.matchar.2018.03.033.
[24] Z. Wang, X. Wang, X. Chen, C. Qiu, Complete columnar-to-equiaxed transition and significant grain refinement in an aluminium alloy by adding Nb particles through laser powder bed fusion, Additive Manufacturing. 51 (2022) 102615. https://doi.org/10.1016/j.addma.2022.102615.
[25] M. Roscher, S. Balachandran, D. Mayweg, E. Jägle, Development of Al-Ti-based alloys for laser powder bed fusion, Additive Manufacturing. 47 (2021) 102315. https://doi.org/10.1016/j.addma.2021.102315.
[26] L. Zhou, H. Hyer, S. Park, H. Pan, Y. Bai, K.P. Rice, Y. Sohn, Microstructure and mechanical properties of Zr-modified aluminum alloy 5083 manufactured by laser powder bed fusion, Additive Manufacturing. 28 (2019) 485–496. https://doi.org/10.1016/j.addma.2019.05.027.
[27] A. Mehta, L. Zhou, T. Huynh, S. Park, H. Hyer, S. Song, Y. Bai, D.D. Imholte, N.E. Woolstenhulme, D.M. Wachs, Y. Sohn, Additive manufacturing and mechanical properties of the dense and crack free Zr-modified aluminum alloy 6061 fabricated by the laser-powder bed fusion, Additive Manufacturing. 41 (2021) 101966. https://doi.org/10.1016/j.addma.2021.101966.

[28] J. Bi, Z. Lei, Y. Chen, X. Chen, Z. Tian, J. Liang, X. Zhang, X. Qin, Microstructure and mechanical properties of a novel Sc and Zr modified 7075 aluminum alloy prepared by selective laser melting, Materials Science and Engineering: A. 768 (2019) 138478. https://doi.org/10.1016/j.msea.2019.138478.
[29] P. ELOI, Mise en œuvre d'alliage d'aluminium 6061 par procédé de Selective Laser Melting, Ecoles des Mines de Saitn Etienne, n.d. https://tel.archives-ouvertes.fr/tel-03537233/document.
[30] P. ELOI, SARNO, Claude, Poudre d'alliage d'aluminium pour fabrication additive, et procédé de fabrication d'une pièce par fabrication à partir de cette poudre, 2017/12/26, 2019.
[31] M.W. Zandbergen, Q. Xu, A. Cerezo, G.D.W. Smith, Study of precipitation in Al–Mg–Si alloys by Atom Probe Tomography I. Microstructural changes as a function of ageing temperature, Acta Materialia. 101 (2015) 136–148. https://doi.org/10.1016/j.actamat.2015.08.017.
[32] X. Xu, Z. Yang, Y. Ye, G. Wang, X. He, Effects of various Mg/Si ratios on microstructure and performance property of Al-Mg-Si alloy cables, Materials Characterization. 119 (2016) 114–119. https://doi.org/10.1016/j.matchar.2016.07.011.
[33] G. Meyruey, V. Massardier, W. Lefebvre, M. Perez, Over-ageing of an Al-Mg-Si alloy with silicon excess, Materials Science and Engineering: A. 730 (2018) 92–105. https://doi.org/10.1016/j.msea.2018.05.094.
[34] B 209 Comittee, Standard Specification for Aluminum and Aluminum-Alloy Sheet and Plate (Metric), ASTM International, n.d. https://www.astm.org/b0209m-10.html.
[35] A.B. Spierings, M. Schneider, R. Eggenberger, Comparison of density measurement techniques for additive manufactured metallic parts, Rapid Prototyping Journal. 17 (2011) 380–386. https://doi.org/10.1108/13552541111156504.
[36] C.A. Schneider, W.S. Rasband, K.W. Eliceiri, Historical commentary NIH Image to ImageJ : 25 years of image analysis, Nature Methods. 9 (2012) 671–675. https://doi.org/10.1038/nmeth.2089.
[37] E.F. Rauch, M. Véron, Automated crystal orientation and phase mapping in TEM, Materials Characterization. 98 (2014) 1–9. https://doi.org/10.1016/j.matchar.2014.08.010.
[38] E.F. Rauch, M. Véron, Methods for orientation and phase identification of nano-sized embedded secondary phase particles by 4D scanning precession electron diffraction, Acta Crystallographica Section B: Structural Science, Crystal Engineering and Materials. 75 (2019). https://doi.org/10.1107/S2052520619007583.
[39] P.G. Klemens, R.K. Williams, Thermal conductivity of metals and alloys, International Metals Reviews. 31 (1986) 196–215.
[40] M. Mujahid, N.N. Engel, E.H. Chia, Effect of alloying elements on the conductivity of aluminum alloys, Scripta Metallurgica. 13 (1979) 887–893. https://doi.org/10.1016/0036-9748(79)90181-9.
[41] S. Patel, M. Vlasea, Melting Modes in Laser Powder Bed Fusion, Materialia. (2020) 100591. https://doi.org/10.1016/j.mtla.2020.100591.
[42] D. Bardel, M. Perez, D. Nelias, A. Deschamps, C.R. Hutchinson, D. Maisonnette, T. Chaise, J. Garnier, F. Bourlier, Coupled precipitation and yield strength modelling for non-isothermal treatments of a 6061 aluminium alloy, Acta Materialia. 62 (2014) 129–140. https://doi.org/10.1016/j.actamat.2013.09.041.
[43] D. Maisonnette, M. Suery, D. Nelias, P. Chaudet, T. Epicier, Effects of heat treatments on the microstructure and mechanical properties of a 6061 aluminium alloy, Materials Science and Engineering: A. 528 (2011) 2718–2724. https://doi.org/10.1016/j.msea.2010.12.011.
[44] H. Westengen, N. Ryum, Precipitation Reactions in an Aluminium 1 wt.% Mg,Si Alloy, International Journal of Materials Research. 70 (1979) 528. https://doi.org/10.1515/ijmr-1979-700810.
[45] T. Bonhoff, M. Poppe, J. Stollenwerk, J.H. Schleifenbaum, P. Loosen, Multi-physical analysis of thermo-optical effects for different Selective Laser Melting (SLM) scanning strategies, Procedia CIRP. 74 (2018) 97–101. https://doi.org/10.1016/j.procir.2018.08.048.
[46] B07 Committee, Specification for Aluminum-Alloy 6061-T6 Standard Structural Profiles, ASTM International, n.d. https://doi.org/10.1520/B0308_B0308M-10.

[47] Standard Specification for Aluminum and Aluminum-Alloy Drawn Tube and Pipe for General Purpose Applications, ASTM International, n.d.
[48] Y. Du, Y.A. Chang, B. Huang, W. Gong, Z. Jin, H. Xu, Z. Yuan, Y. Liu, Y. He, F.-Y. Xie, Diffusion coefficients of some solutes in fcc and liquid Al: critical evaluation and correlation, Materials Science and Engineering: A. 363 (2003) 140–151. https://doi.org/10.1016/S0921-5093(03)00624-5.
[49] K.E. Knipling, D.C. Dunand, D.N. Seidman, Criteria for developing castable, creep-resistant aluminum-based alloys – A review, Z. Metallkd. (2006) 20.
[50] R. Li, M. Wang, Z. Li, P. Cao, T. Yuan, H. Zhu, Developing a high-strength Al-Mg-Si-Sc-Zr alloy for selective laser melting: Crack-inhibiting and multiple strengthening mechanisms, Acta Materialia. 193 (2020) 83–98. https://doi.org/10.1016/j.actamat.2020.03.060.
[51] R.A. Michi, A. Plotkowski, A. Shyam, R.R. Dehoff, S.S. Babu, Towards high-temperature applications of aluminium alloys enabled by additive manufacturing, International Materials Reviews. 67 (2022) 298–345. https://doi.org/10.1080/09506608.2021.1951580.
[52] J. Banhart, C.S.T. Chang, Z. Liang, N. Wanderka, M.D.H. Lay, A.J. Hill, Natural Aging in Al-Mg-Si Alloys - A Process of Unexpected Complexity, Adv. Eng. Mater. 12 (2010) 559–571. https://doi.org/10.1002/adem.201000041.
[53] F. De Geuser, W. Lefebvre, D. Blavette, 3D atom probe study of solute atoms clustering during natural ageing and pre-ageing of an Al-Mg-Si alloy, Philosophical Magazine Letters. 86 (2006) 227–234. https://doi.org/10.1080/09500830600643270.
[54] P. Dumitraschkewitz, P.J. Uggowitzer, S.S.A. Gerstl, J.F. Löffler, S. Pogatscher, Size-dependent diffusion controls natural aging in aluminium alloys, Nat Commun. 10 (2019) 4746. https://doi.org/10.1038/s41467-019-12762-w.
[55] M. Madanat, M. Liu, J. Banhart, Reversion of natural ageing in Al-Mg-Si alloys, Acta Materialia. 159 (2018) 163–172. https://doi.org/10.1016/j.actamat.2018.07.066.
[56] W. Lefebvre, G. Rose, P. Delroisse, E. Baustert, F. Cuvilly, A. Simar, Nanoscale periodic gradients generated by laser powder bed fusion of an AlSi10Mg alloy, Materials & Design. 197 (2021) 109264. https://doi.org/10.1016/j.matdes.2020.109264.
[57] F. Stadler, H. Antrekowitsch, W. Fragner, H. Kaufmann, E.R. Pinatel, P.J. Uggowitzer, The effect of main alloying elements on the physical properties of Al–Si foundry alloys, Materials Science and Engineering: A. 560 (2013) 481–491. https://doi.org/10.1016/j.msea.2012.09.093.